ADVANCED FUNCTIONAL MATERIALS
www.afm-journal.de

Heterogeneous Integration of Compact Perovskite Films on Pixelated Arrays via Solid-State Crystal Growth for X-Ray Imaging

Tongyu Shi, Jie Kang, Yang Zhang, Wenxuan Yang, Xingzhou Su, Zhiyuan Liu, Xiaoli Wang, Dong Li, Xingchen He, Paul K. Chu, Yanliang Liu, and Xue-Feng Yu**

Metal halide perovskites are promising candidates for direct X-ray imaging, but their heterogeneous integration with pixelated sensing arrays remains challenging. Herein, a novel solid-state crystal growth strategy to integrate high-quality perovskites with the pixelated electrode substrate for X-ray imaging is described, and the soft methylammonium lead triiodide solvate ($MAPbI_3$•DMF) powder is utilized as precursor and is soft-pressed directly on the thin film transistor (TFT) array at moderate pressure and temperature (100 °C, 0.8 MPa) instead of common perovskite suspension printing. A compact and dense $MAPbI_3$ thick film is obtained with excellent mobility-lifetime ($\mu\tau$) of 1.92×10^{-3} $cm^2 \bullet V^{-1}$. The X-ray detector shows a high sensitivity of 40,970 $\mu C \bullet Gy_{air}^{-1} \bullet cm^{-2}$ and a low detection limit of 14.3 $nGy_{air} \bullet s^{-1}$. In addition, the TFT perovskite X-ray flat-panel exhibits a well-distributed pixel response and high spatial resolution of 0.6 $lp \bullet pixel^{-1}$ for X-ray imaging.

1. Introduction

X-ray imaging panels have broad applications in medical imaging, industrial nondestructive inspection, and security checks. In recent years, metal halide perovskites, including single crystal,[1] polycrystalline wafers,[2,3] and thick film[4] have shown potential in direct X-ray detection due to the large X-ray attenuation coefficient, high carrier mobility (μ), long carrier lifetime (τ), and high defect tolerance.[5–7] Direct X-ray detectors based on perovskite semiconductors have high detection sensitivity of more than 1×10^5 $\mu C \bullet Gy_{air}^{-1} \bullet cm^{-2}$ and low detection-limited X-ray dose rates of few $nGy_{air} \bullet s^{-1}$, which are significantly higher than those of commercial amorphous selenium (a-Se) X-ray detectors and comparable to those of expensive cadmium zinc telluride (CZT) detectors.[8,9] To achieve high-resolution X-ray imaging, perovskite semiconductors must be integrated into pixel chip arrays such as TFT and CMOS containing amplifiers, storage capacitors, and readout circuits.[10] Hence, the chip integration-compatible processing techniques for compact and uniform perovskite thick layers are crucial to the fabrication of X-ray imaging panels.

In general, solution-processed perovskite thick films for X-ray imaging are prepared by printing the perovskite suspension on the large-area TFT array.[5,11] In order to obtain hundreds of micrometers thick perovskite films for sufficient X-ray absorption, the utilized perovskite suspension usually contains excessive particles and supersaturated solution with uneven distribution of particles and solutes, consequently resulting in uncontrollable nucleation and growth of crystals in perovskite thick film fabrication. The resulting perovskite thick films suffer from a mount of crystal defects and severe ion migration, leading to undesired energy recombination loss and dark currents.[12] In addition, after solvent evaporation, vast amounts of pores and pinholes are inevitably produced in the perovskite layer which inhibits X-ray absorption and charge transport.[11] Consequently, the pixel-level uniformity of the perovskite layer seriously affects the spatial resolution of perovskite X-ray imaging panels.[13,14] Polymerizable additives and soft-pressing strategies have been developed to partly ameliorate the discontinuity and heterogeneity of solution-processed perovskite thick films,[11,14] but the insulating additives inevitably impair the charge carrier transmission and photoelectric response of X-ray detectors. Therefore, the integration of

T. Shi, J. Kang, Y. Zhang, W. Yang, X. Su, Z. Liu, X. Wang, D. Li, X. He, Y. Liu, X.-F. Yu
Shenzhen Institute of Advanced Technology
Chinese Academy of Sciences
Shenzhen, Guangdong 518055, China
E-mail: yl.liu4@siat.ac.cn; xf.yu@siat.ac.cn
T. Shi, Y. Liu, X.-F. Yu
University of Chinese Academy of Sciences
Beijing 100049, China
P. K. Chu
Department of Physics
Department of Materials Science and Engineering and Department of Biomedical Engineering
City University of Hong Kong
Tat Chee Avenue, Kowloon, Hong Kong 999077, China
Y. Liu, X.-F. Yu
Key Laboratory of Biomedical Imaging Science and System
Chinese Academy of Sciences
Shenzhen, Guangdong 518055, China

The ORCID identification number(s) for the author(s) of this article can be found under https://doi.org/10.1002/adfm.202421569

DOI: 10.1002/adfm.202421569

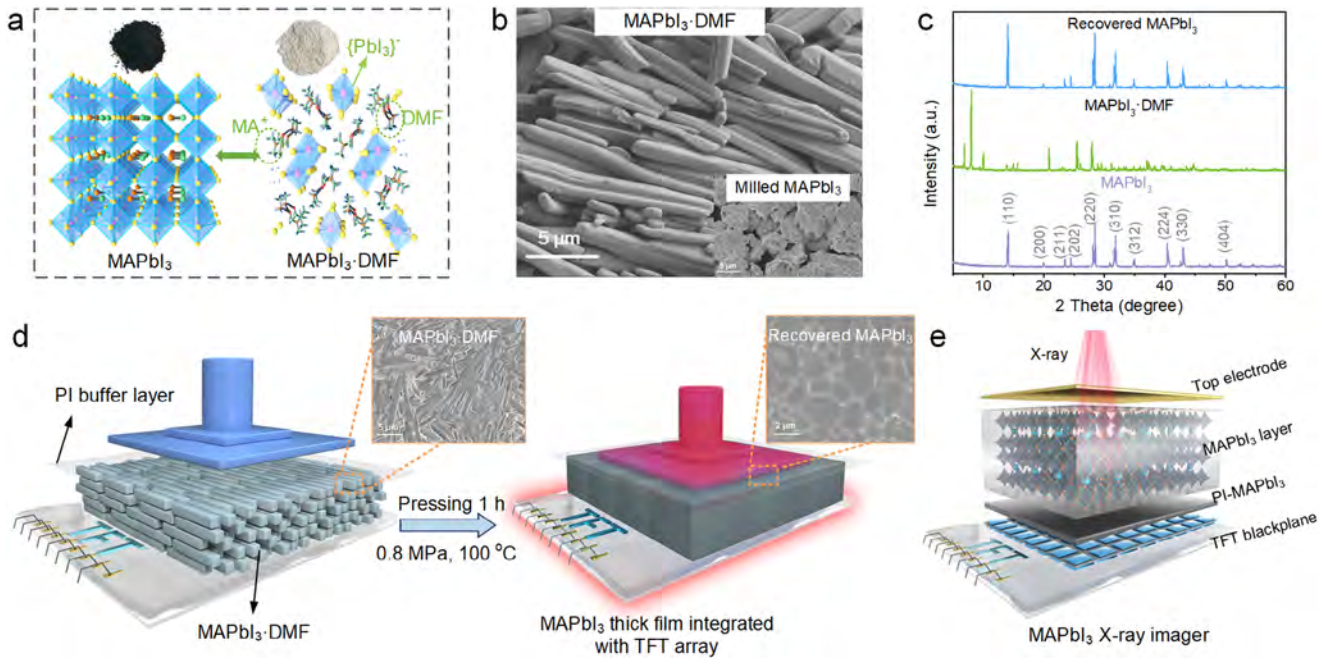

Figure 1. $MAPbI_3$·DMF preparation and integration with the TFT array. a) Crystal formation of $MAPbI_3$ and $MAPbI_3$·DMF solvate (inset: photograph of $MAPbI_3$ and $MAPbI_3$·DMF powder). b) SEM image of $MAPbI_3$·DMF (inset: SEM image of milled $MAPbI_3$ powder). c) XRD patterns of ball-milled $MAPbI_3$, $MAPbI_3$·DMF and recovered $MAPbI_3$ solvate. d) Process diagram of heterogeneous integration of perovskites with the TFT array through soft-pressing $MAPbI_3$·DMF. e) Diagram of the perovskite X-ray imaging panel.

perovskite thick film onto pixelated arrays for X-ray imaging faces formidable obstacles.

Herein, a novel solid-state crystal growth strategy is developed to achieve heterogeneous integration of the compact perovskite thick film on the TFT array. The soft methylammonium lead triiodide solvate ($MAPbI_3$•DMF) powder is utilized as the precursor instead of the perovskite suspension to avoid the excessive solution effects on the perovskite crystal growth, and it is pressed directly onto the thin film transistor (TFT) array at moderate pressure and temperature (100 °C, 0.8 MPa) without damaging the TFT glass substrate. A compact and dense $MAPbI_3$ thick film with excellent mobility-lifetime ($\mu\tau$) of 1.92×10^{-3} cm^2•V^{-1} is obtained on the TFT array. The X-ray detector shows a high sensitivity of 40970 μC•Gy_{air}^{-1}•cm^{-2} and a low detection limit of 14.3 nGy_{air}•s^{-1}, and the TFT X-ray imaging panel exhibits a well-distributed pixel response and high spatial resolution of 0.6 lp•$pixel^{-1}$.

2. Fabrication and Investigation of the $MAPbI_3$ Thick Film

The $MAPbI_3$•DMF can be synthesized by placing the $MAPbI_3$ powder in a DMF/chlorobenzene mixture (see Experimental Section and Figure S1, Supporting Information for more details). As shown in **Figure 1**a,b, the white $MAPbI_3$•DMF powder exhibits a regular rod-like shape with the predominant configuration of a 1D edge-sharing long chain separated by MA^+ ions and DMF molecules.[15,16] Figure 1b inset and Figure S2 (Supporting Information) show the contrast with the ball-milled black perovskite particles with an irregular shape and size. A series of perovskite solvates are formed by lattice expansion of perovskites along the *c*-axis arising from the intercalation of the solvent molecule, including intermolecular hydrogen bonding (N—H...O═C asymmetric bifurcated bond)[15] and coordination interaction between the oxygen lone pair electrons in the solvent and Pb(II) (Figures S3 and S4, Supporting Information).[9,17] The XRD patterns of $MAPbI_3$·DMF exhibit several typical peaks below 10° ($2\theta = 6.49°$, 6.90°, 8.05°, 9.49°). After annealing, it is converted back into black $MAPbI_3$ powders, as shown in Figure 1c, and it is confirmed by the thermogravimetric analysis. The $MAPbI_3$·DMF starts to lose weight at 58 °C and is converted into $MAPbI_3$·at 110 °C (Figure S5, Supporting Information). The $MAPbI_3$·DMF only loses ≈10% of its weight to form recovered $MAPbI_3$, which is able to avoid the excessive solution effects on the perovskite crystal growth. Besides, a series of perovskite solvates can be obtained by the same process (Figures S6 and S7, Supporting Information). In addition, the released DMF vapor promotes perovskite crystal growth, and the recovered $MAPbI_3$ shows a higher XRD peak intensity than the pristine $MAPbI_3$ powder.

The rod-shaped $MAPbI_3$•DMF powder is pressed directly onto the TFT array at a low pressure of 0.8 MPa to fabricate the thick $MAPbI_3$ film, as shown in Figure 1d. The $MAPbI_3$•DMF has significantly lower Young's modulus than $MAPbI_3$ according to atomic force microscopy (Figure S8, Supporting Information), and so $MAPbI_3$•DMF is prone to deformation at this pressure. Owing to the flexibility, processability, and regrowth capabilities of the $MAPbI_3$•DMF powder, the $MAPbI_3$ thick film can be fabricated by soft-pressing the $MAPbI_3$•DMF powder at compatible pressure and temperature without damaging the TFT array, thus achieving the heterogeneous integration of $MAPbI_3$ onto the TFT pixel array (Figure 1d; Figure S9, Supporting Information). The fabrication of the $MAPbI_3$ thick film is described in the

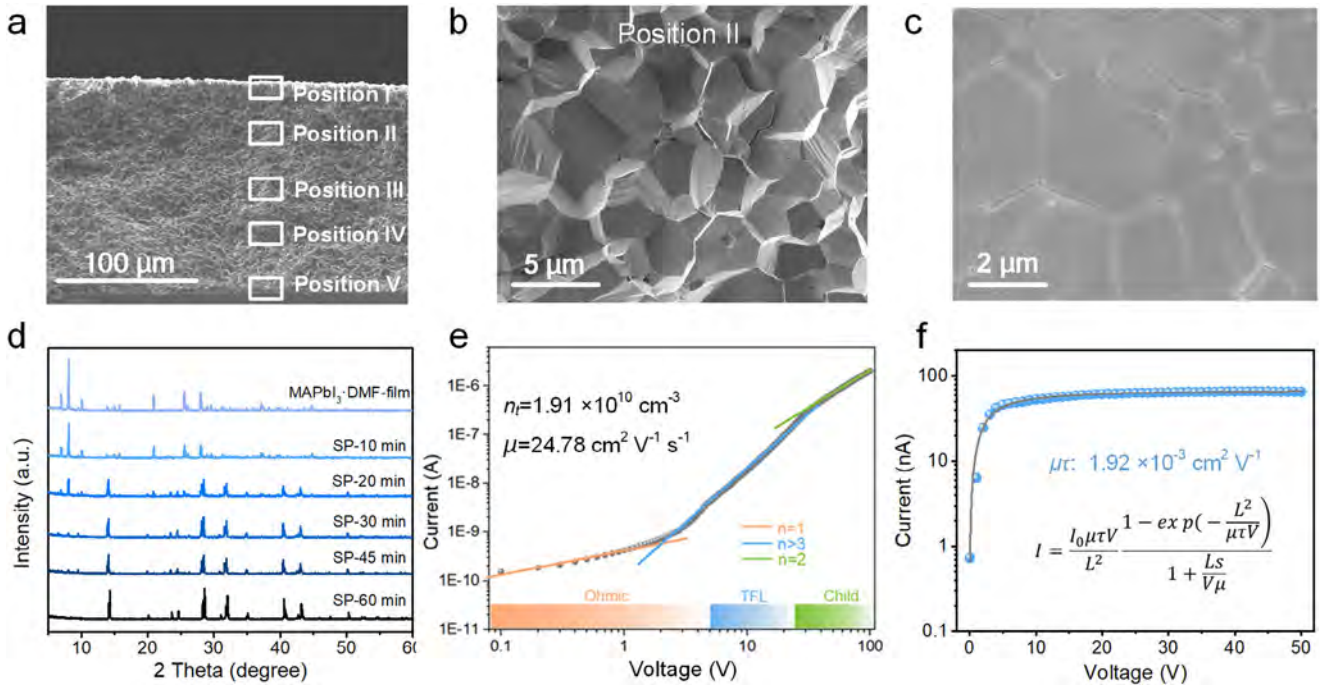

Figure 2. Characterization of $MAPbI_3$ thick film. a,b) Cross-sectional SEM images of $MAPbI_3$ thick film. c) Surface SEM image of $MAPbI_3$ thick film. d) Structural evolution of the $MAPbI_3$ film at different soft pressing (SP) times from the beginning to 1 h. e) *I–V* curve of 500-μm perovskite thick film. f) Photoconductivity and Hecht equation fitted curve.

experiment section. The Au electrode is deposited on the $MAPbI_3$ thick film to form the TFT-based perovskite X-ray imaging panel, as shown in Figure 1e.

The $MAPbI_3$· DMF-assisted soft-pressed $MAPbI_3$ thick film exhibits a dense and compact morphology both on the inside and surface, as shown in **Figure** 2a–c, in contrast to the porous and uneven solution-processed $MAPbI_3$ thick film prepared with the blade coating perovskite suspension (Figure S10, Supporting Information). The cross-section also shows a dense and uniform morphology with large grain size and few grain boundaries, which is beneficial for efficient X-ray absorption and charge transport (Figure S11, Supporting Information). Time-dependent morphological evolution of the soft-pressed $MAPbI_3$·DMF thick film was analyzed by SEM imaging of discrete samples processed for 10–60 min (Figure S12, Supporting Information). The initial $MAPbI_3$·DMF film shows a closely aligned rod-shaped morphology, but after annealing, the $MAPbI_3$·DMF solvate is gradually converted into small $MAPbI_3$ grains and DMF vapor. The released DMF vapor promotes $MAPbI_3$ crystal growth, and the adjacent small $MAPbI_3$ grains merge with each other. Ultimately, the rod-shaped $MAPbI_3$·DMF disappears, resulting in a $MAPbI_3$ thick film with a large grain size and compact morphology, as shown in Figure 2c. The transformation of $MAPbI_3$·DMF into the complete $MAPbI_3$ thick film is also monitored by time-dependent XRD as shown in Figure 2d. During hot pressing, the typical diffraction peaks (2θ <10°) of $MAPbI_3$·DMF weaken gradually and then disappear. Meanwhile, the diffraction peaks of $MAPbI_3$ continue to increase, indicating the conversion from $MAPbI_3$·DMF to the complete $MAPbI_3$ thick film. A series of $MAPbI_3$ thick films with various thicknesses from 115 to 485 μm are fabricated by controlling the mass of the soft-pressed $MAPbI_3$·DMF powder and/or the number of lamination cycles (Figure S13, Supporting Information). The untreated $MAPbI_3$ particles are also directly pressed onto the glass using the same parameters, and the $MAPbI_3$ film exhibits a loose structure and cannot be integrated into the substrate (Figure S14, Supporting Information), thereby verifying the indispensable role of the $MAPbI_3$·DMF powder in the heterogeneous integration of the compact $MAPbI_3$ thick film on the substrate.

The photoelectric properties of the $MAPbI_3$ thick film are determined by space charge-limited current (SCLC) measurements as shown in Figure 2e. The defect state density is determined by the trap filling threshold voltage (V_{TFL}) as shown in the following:

$$n_t = \frac{2\varepsilon\varepsilon_0 V_{TFL}}{eL^2} \tag{1}$$

where ϵ_0 represents the vacuum permittivity, ϵ is the dielectric constant (ϵ = 21.2 for $MAPbI_3$[18]), e denotes the charge of an electron, and L is the thickness. The $MAPbI_3$ thick film exhibits an extraordinarily low trap density of 1.91×10^{10} cm^{-3} compared to the control group and previous reports (Figure S15, Supporting Information).[19] The carrier mobility (μ) can be determined by analyzing the dark current density-voltage (*J–V*) characteristics according to the Mott–Gurney equation:

$$J_D = \frac{9}{8}\varepsilon\varepsilon_0\mu\frac{V^2}{L^3} \tag{2}$$

where J_D is the dark current density, and V stands for the applied bias voltage. By fitting the $J \propto V^2$ curve, the calculated carrier mobility is 23.42 $cm^2 \cdot V^{-1} \cdot s^{-1}$, comparable to that of the $MAPbI_3$

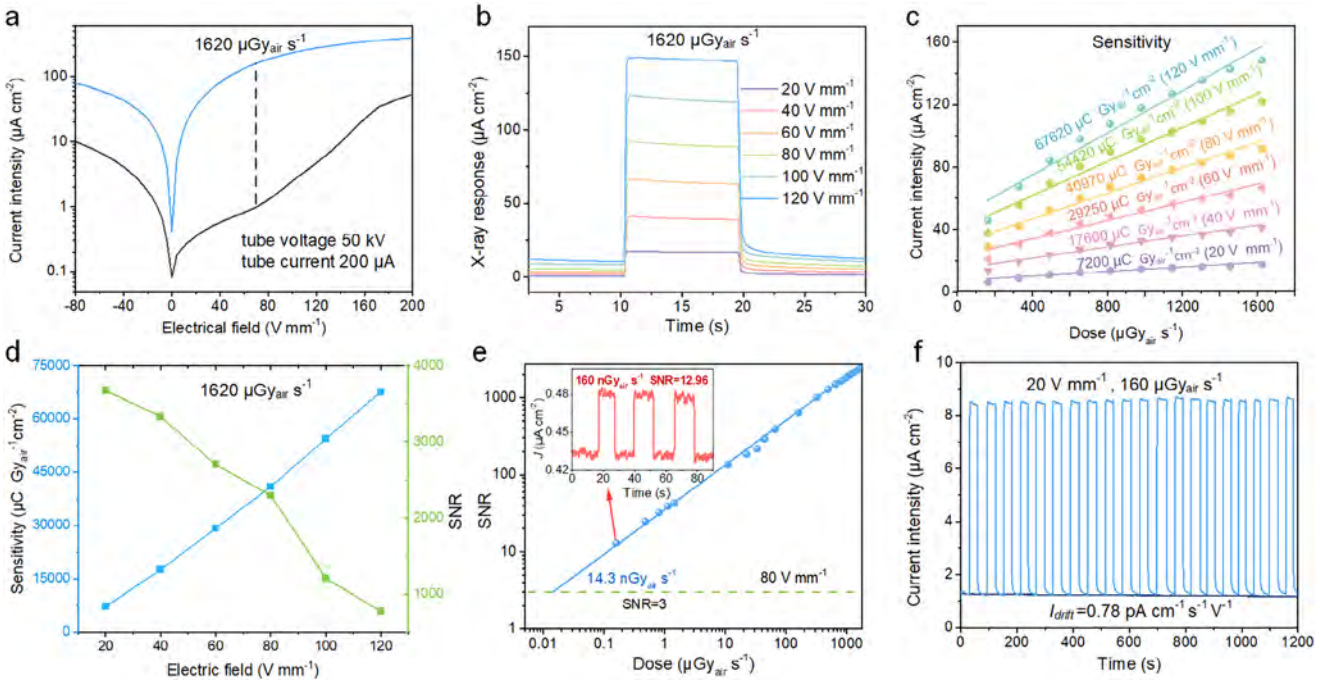

Figure 3. The X-ray detection performance of the soft-pressed $MAPbI_3$ thick film. a) *J–V* curves of the X-ray detector under dark conditions (dark) and X-ray radiation (blue). b) X-ray response of the $MAPbI_3$ detector at different biases. c) Sensitivity: X-ray current densities as a function of dose rates. d) Variations of the material sensitivity and SNR for different electric fields. e) Dose rate-dependent SNR ratios of the device. (Inset: *J–V* curve of the $MAPbI_3$ detector under the dose of 160 $nGy_{air} \bullet s^{-1}$.) f) *J-T* curve under alternating on-off X-ray radiation and darkness for 1200 s.

single crystal.[20] The Hecht equation is commonly used to fit the photocurrent-voltage curve under illumination to determine the $\mu\tau$ product (Figure 2f). The $\mu\tau$ product of the dense $MAPbI_3$ film is calculated to be 1.92×10^{-3} $cm^2 \cdot V^{-1}$, which is almost twenty times larger than that of the printed $MAPbI_3$ (1.0×10^{-4} $cm^2 \cdot V^{-1}$).[5]

The soft-pressed $MAPbI_3$ thick film shows significantly enhanced photoluminescence (PL) intensity and redshifted absorb peak compared to conventional solution-processed perovskite thick film (Figure S16, Supporting Information). Time-resolved photoluminescence (TRPL) measurements were conducted starting at 160 K to investigate the dynamic processes of charge carriers in halide perovskites. As shown in Figure S17 (Supporting Information), we performed a biexponential fitting analysis of the measured curves, while the short component (τ_1) reflects the presence of defect states, and the long lifetime (τ_2) component represents radiative recombination.[21] Observing from the control group, τ_1 significantly increased with rising temperature, indicating thermal activation of defects. In contrast, our hot-pressed thick films showed relatively less temperature dependence compared to the control group, suggesting a higher defect tolerance and better film quality.[22] The surface potential of the $MAPbI_3$ thick film is analyzed by Kelvin probe force microscopy (KPFM) (Figure S18, Supporting Information). The soft-pressed $MAPbI_3$ thick film exhibits obviously lower electrical potential than the solution-processed sample. Considering that ions are easy to migrate under a bias voltage, resulting in a high potential, the lower electrical potential of the soft-pressed $MAPbI_3$ thick film indicates reduced ion migration.[3,23]

3. X-Ray Detection

The X-ray detector based on soft-pressed $MAPbI_3$ thick film is fabricated with a device configuration of ITO/PI-$MAPbI_3$/$MAPbI_3$/Au to evaluate the X-ray detection performance. Based on ultraviolet photoemission spectroscopy (UPS) and reflectance spectroscopy (Figure S19, Supporting Information), the valence band maximum and conduction band minimum are determined to be −5.45 and −3.94 eV, respectively. In the current density versus voltage (*J–V*) curve in **Figure 3a**, the X-ray detector shows a rectifying behavior, and the Schottky contact between perovskites and Au/ITO electrodes is beneficial to reducing the dark current.[5] The maximum dark-to-light current switch ratio is 164 at an electric field of 68 $V \bullet mm^{-1}$. It also shows rapid response and stable baselines to X-ray at various biases, as shown in Figure 3b. The photocurrent density exhibits a linear relationship with the X-ray dose rate within the range of 160 to 1620 $\mu Gy_{air} \bullet s^{-1}$ (Figure S20, Supporting Information). By calculating the slope, the sensitivities of the X-ray detector under 20, 40, 60, 80, 100, and 120 $V \bullet mm^{-1}$ are determined to be 7200, 17600, 29250, 40970, 54420, and 67620 $\mu C \bullet Gy_{air}^{-1} \bullet cm^{-2}$, respectively, as shown in Figure 3c. Notably, these values significantly surpass those of previously reported $MAPbI_3$-based X-ray detectors, thereby confirming the superior quality of the soft-pressed dense and compact $MAPbI_3$ thick film (Figure S21, Supporting Information).

Based on the noise calculated from the standard deviation of the photocurrent, the signal-to-noise ratios (SNR) of the X-ray detector at various electric fields are calculated and shown in Figure 3d. The SNR decreases with increasing electric field, and

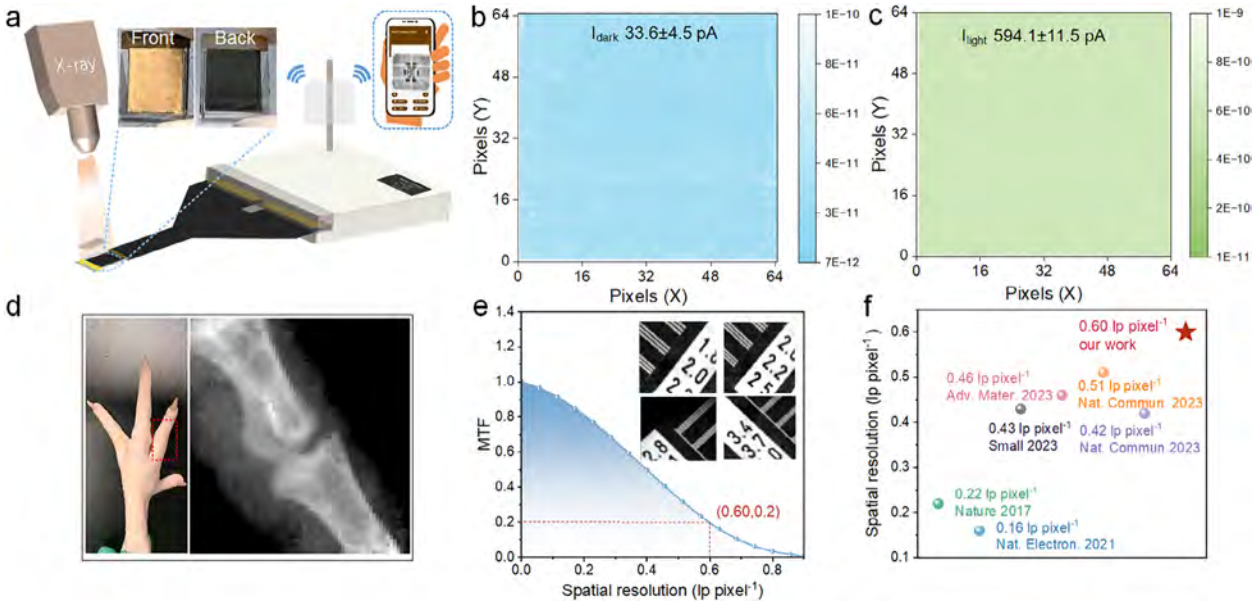

Figure 4. X-ray imaging panel properties. a) Schematic illustration of the perovskite X-ray imaging panel (Inset: front and back photo images of the $MAPbI_3$ X-ray imaging panel). b) Dark current and c) Photocurrent distribution of the X-ray imaging panel. d) Photograph and X-ray imaging of the chicken foot. e) MTF curve of the perovskite X-ray imaging panel and X-ray images of the line pair card. f) Summary of the reported spatial resolution of the perovskite X-ray imaging panel.

the comprehensive device performance is assessed at an electric field of 80 V•mm^{-1}. The detection limit is another crucial indicator, as defined by the International Union of Pure and Applied Chemistry (IUPAC), which is the equivalent dose rate required to generate a signal three times the magnitude of the noise level.[24] The SNR to X-ray dose rate curve is plotted in Figure 3e. Assuming the minimum SNR of 3, the detection limit is determined to be 14.3 nGy_{air}•s^{-1}, thus verifying the low-dose X-ray detection capability. At a dose rate of 32 nGy_{air} s^{-1}, the SNR was measured to be 5.4, which is indeed close to the detection limit (Figure S22, Supporting Information). The stability of the X-ray detector is evaluated under operating conditions, as shown by cyclic experiments conducted under alternate on-off X-ray radiation in Figure 3f. Overall, the detector exhibits a relatively stable response with minimal attenuation in both dark current and photocurrent during the testing period showing an accumulating radiation dose of up to 192 mGy. The dark current drift velocity is only 0.78 pA•cm^{-1}•s^{-1}•V^{-1} after continuous operation for 1200 s. Moreover, the long-term tested $MAPbI_3$ thick film exhibits a comparable XRD pattern with the original $MAPbI_3$ thick film, which indicates the crystal structure of the $MAPbI_3$ perovskites is stable under constant X-ray irradiation (Figure S23, Supporting Information). In addition, a large-size soft-pressed $MAPbI_3$ thick film (8 × 8 cm) was successfully prepared with uniform morphology. Five randomly selected areas are chosen to record dark current-voltage curves, and excellent consistency is observed (Figure S24, Supporting Information), indicating the detector can mass produced commercially.

4. X-Ray Imaging

The X-ray imaging panel is fabricated by solid-state integration of the $MAPbI_3$ thick film with the TFT array by soft-pressing the $MAPbI_3$·DMF powder as illustrated in **Figure** 4a. The TFT array has 64 × 64 pixels (200 μm) with an active area of 12.8 × 12.8 mm^2 (Figure S25, Supporting Information), and the flexible printed circuits consisting of gate drive integrated circuits and readout chips are bonded thermally onto the TFT array for image readout (Figure S26, Supporting Information). Upon X-ray irradiation, holes are driven by the external bias and collected by the storage capacitor, and the digital image signals are generated by the analog-to-digital converter (Figures S27 and S28, Supporting Information). The uniformity of the perovskite TFT pixels directly affects the quality of X-ray imaging. In order to investigate the uniformity of the imaging panel, we calculate the dark current and photocurrent distribution of the 64 × 64 pixels in Figure 4b,c and Figure S29 (Supporting Information). The perovskite TFT pixels exhibit a dark current of 33.6±4.5 pA and a photocurrent of 594.1±11.5 pA under X-ray illumination. It is worth noting that the standard deviations of both dark and photocurrents are significantly lower than that of the signal currents, demonstrating excellent uniformity. Furthermore, we visually demonstrate the imaging capability of the X-ray imaging panel using a mobile phone memory card and ball-point pen under 50 kV X-ray irradiation (Figure S30, Supporting Information). The contours of the pen and memory card can be clearly distinguishable without damaging the object, confirming the excellent imaging capability and potential for industrial nondestructive testing. Besides, a chicken foot is imaged to demonstrate high-resolution biomedical imaging. The knuckles of the chicken foot can be clearly observed, and the outside is covered with muscles, as shown in Figure 4d.

The modulation transfer function (MTF), which represents the spatial resolution or relative response as a function of spatial frequency, is a crucial parameter to assess the detector performance. As illustrated in Figure 4e, the MTF is measured using

the knife-edge method. For MTF = 0.2, the X-ray imaging panel achieves a higher spatial resolution of 0.6 lp•pixel^{-1} than that of previously reported perovskite X-ray imagers,[5,6,13,14,25] as shown in Figure 4f, which is attributed to the soft-pressed, dense, and uniform $MAPbI_3$ thick film as well TFT array pixels. Additionally, the spectral lines with a resolution of 3.1 lp•mm^{-1} of the standard line pair card can be discerned upon X-ray irradiation (Figure S31 and Table S1, Supporting Information), which is consistent with the resolution obtained from the MTF curve. These results indicate the high potential of the soft-pressed $MAPbI_3$ X-ray imaging panel in nondestructive testing and medical imaging.

5. Conclusion

A solid-state crystal growth strategy is demonstrated to integrate compact $MAPbI_3$ thick film on the TFT array for X-ray imaging. Rod-shaped $MAPbI_3$•DMF solvate powders with soft properties are employed as the precursor instead of a perovskite suspension in the preparation of the $MAPbI_3$ thick film, which can be soft-pressed directly onto the TFT array at compatible pressure and temperature without damaging the TFT substrate. This technique avoids the adverse effects of excessive solution on perovskite crystal growth, resulting in the production of a dense and uniform $MAPbI_3$ thick film with high crystallinity, suppressed ion migration, and excellent charge carrier properties ($\mu\tau$ product of 1.92×10^{-3} cm^2 V^{-1}). The obtained $MAPbI_3$ thick film not only has satisfactory photoelectric properties comparable to perovskite single crystals but also scalable size and thickness, thus boding well for X-ray detection and imaging. The X-ray detector has a high sensitivity of 40970 μC•Gy_{air}^{-1}•cm^{-2} and a low detection limit of 14.3 nGy_{air}•s^{-1}. The X-ray imaging panel fabricated on the TFT array exhibits a near-to-limit spatial resolution of 0.6 lp•pixel^{-1}. Compared to solution-processed methods, the solid-state crystal growth strategy avoids the excessive solution effects on perovskite crystal growth and paves the way for the design of next-generation direct X-ray imaging technology.

6. Experimental Section

Materials: Methylammonium iodide (MAI, >99.99%), methylammonium bromide (MABr, >99.99%), and formamidinium iodide (FAI, >99.99%) were purchased from Great Solar Cell. Lead iodide (PbI_2) (99.999%), lead bromide ($PbBr_2$) (99.9%), Dimethyl Formamide (DMF, AR, 99.9%), dimethyl sulfoxide (DMSO, AR, 99%), chlorobenzene (CB, AR, 99%), and γ-butyrolactone (GBL) were bought from Aladdin. 1,2,4,5-Benzenetetracarboxylic anhydride (PMDA, 98%) and 4,40-oxybisbenzenamine (ODA, 98%) were obtained from Energy Chemical. All the chemicals were used as received without any further purification.

Perovskite Solvate Synthesis: The $MAPbI_3$ powder was synthesized by grinding MAI and PbI_2 with a stoichiometric ratio 1:1 using a planetary ball mill (XHXQM-4L, MITR) for 30 min at 400 rpm. 0.340 g of MAI and 1.004 g of PbI_2 were mixed in an agate jar ball with a volume of 100 mL and 16 agate balls (diameter size 5 mm) to prepare the $MAPbI_3$ powder. 1 g of the $MAPbI_3$ powder was added to the DMF/ CB mixture (0.2 mL DMF and 2 mL CB) and after stirring for 1 h, the mixture turned colorless. The $MAPbI_3$·DMF powder was obtained by centrifugation and vacuum drying.

Fabrication of X-Ray Imaging Panel: A thin PI-$MAPbI_3$ film was spin-coated on the TFT array at 3000 rpm for 30 s and annealed at 100 °C for 10 min. The PMDA and ODA (1:0.9) were dissolved in DMF (1:9) and stirred overnight in a sealed container at room temperature to prepare the polyamide acid (PAA) solution. The $MAPbI_3$ solution was prepared by mixing 4.61 g of PbI_2 and 1.59 g of MAI in 3 mL of DMF and stirring for 6 h. The $MAPbI_3$ solution and PAA solution were mixed with a volume ratio of 1:1 and stirred overnight at room temperature to obtain the PI-$MAPbI_3$ solution. The $MAPbI_3$·DMF powder was spread evenly on the PI-$MAPbI_3$ layer within a pre-designed mask to fabricate the $MAPbI_3$ thick film. In the soft-pressing process, a PET film was overlaid on the powder to form a hydrophobic buffer layer and compacted for 1 h at 100 °C using a pneumatic hot press machine at a low pressure of 0.8 MPa. Finally, the Au top electrode was thermally deposited on the $MAPbI_3$ thick film in a vacuum oven to produce the TFT-driven X-ray imaging panel. The TFT array and readout system utilized in this study were purchased from LinkZill Technology Co., Ltd., with the model SC-T-A064-2203, which has a pixel count of 64 × 64, and the edge regions accommodate the clock and logic signal pins. The pixel structure of the detector array was 1T1D, where T represents the switch transistor, and D represents the perovskite device. When the clock signal arrives, the TFT gate was activated, and charges are output. The pixel size of the TFT panel was 200 × 200 μm^2, with each pixel connected to a clock signal line and a signal readout line. The readout charge was directly transferred to an external preamplifier with a capacitance of 25 pF. This signal was subsequently processed through an analog-to-digital converter (ADC) and then output to the image processing and storage module. The amplifier and current readout circuits were integrated within commercial Readout Integrated Circuits (ROICs). These ROICs supported a maximum readout rate of 3.1 kSPS, while the readout frame rate for the detector array was ≈8 Hz (≈512 SPS).

Fabrication of Single-Pixel Detector: The soft-pressed $MAPbI_3$ thick film was integrated into the ITO substrate in a similar manufacturing process to the X-ray imaging panel. Subsequently, 100 nm-thick Au electrodes were thermally deposited on the surface of the thick film with a mask, and the electrode area was 0.01 cm^2.

Materials Characterization: The morphology was recorded by scanning electron microscopy (SEM, Zeiss Gemini SEM 300). The composition was examined by energy-dispersive X-ray spectroscopy (EDS) using the accessory manufactured by Oxford Instruments. To characterize the chemical structure, X-ray photoelectron spectroscopy (XPS, Thermo ESCALAB 250Xi) and Fourier-transform infrared spectroscopy (FT-IR, Thermo Scientific, Nicolet iS50) according to the KBr pellet method were carried out. The crystal structure was investigated by powder X-ray diffraction (XRD) on the Rigaku Smartlab 3 kW X-ray diffractometer with Cu K_α radiation. The UV–vis absorption spectra were acquired on the UV–vis spectrometer (UV-1800, Shimadzu). Photoluminescence (PL) and time-resolved photoluminescence (TRPL) were performed on the fluorescent spectrophotometers (Hitachi F-4600 and Edinburgh FLS-1000) using an excitation wavelength of 365 nm. Ultraviolet photoemission spectroscopy (UPS) was carried out on an ESCALAB 250Xi electron spectrometer (Thermo Fisher Scientific) using a monochromatic Al K_α source (300 W). The surface roughness, mechanical properties, and surface potential of the film were determined by atomic force microscopy (AFM, Bruker). For optical response in $\mu\tau$ measurement, a monochromatic LED light (460 nm) was used as the illumination source.

Detector Performance Measurement: The X-ray detection characteristics were evaluated using an X-ray generation system for medical imaging (Varex, G242, 18932-M8, USA). The accelerating voltage was 50 kV, and the currents were varied from 10 to 200 uA. The dose rate of the X-rays was calibrated by the X2 CT dosimeter (Unfors Raysafe, Sweden). During the measurement conducted in darkness, the external electrical bias and current were recorded by the PDA FS380 semiconductor analyzer. The modulation transfer function (MTF) was determined by the slanted-edge method by imaging a sharp edge.

Supporting Information

Supporting Information is available from the Wiley Online Library or from the author.

Acknowledgements

This work was financially supported by the National Key R&D Program of China (2023YFA0915600), the National Natural Science Foundation of China (62474187, 12235006, 22305262), Shenzhen Science and Technology Program Grant (ZDSYS20220527171406014, JCYJ20220818101612027, JCYJ20220531095813031), the Postdoctoral Fellowship Program of CPSF (GZC20241848), Guangdong Basic and Applied Basic Research Foundation (2024A1515012494) and City University of Hong Kong Donation Research Grants (DON-RMG 9229021 and 9220061).

Conflict of Interest

The authors declare no conflict of interest.

Data Availability Statement

The data that support the findings of this study are available from the corresponding author upon reasonable request.

Keywords

dense and compact thick film, heterogeneous integration, high-resolution, $MAPbI_3 \bullet DMF$, perovskite X-ray detection, X-ray imaging

Received: November 7, 2024
Revised: February 20, 2025
Published online: April 9, 2025

[1] a) H. Wei, Y. Fang, P. Mulligan, W. Chuirazzi, H.-H. Fang, C. Wang, B. R. Ecker, Y. Gao, M. A. Loi, L. Cao, *Nat. Photon.* **2016**, *10*, 333; b) J. Jiang, M. Xiong, K. Fan, C. Bao, D. Xin, Z. Pan, L. Fei, H. Huang, L. Zhou, K. J. N. P. Yao, *Nat. Photon.* **2022**, *16*, 575.

[2] S. Shrestha, R. Fischer, G. J. Matt, P. Feldner, T. Michel, A. Osvet, I. Levchuk, B. Merle, S. Golkar, H. Chen, *Nat. Photon.* **2017**, *11*, 436.

[3] W. Liu, T. Shi, J. Zhu, Z. Zhang, D. Li, X. He, X. Fan, L. Meng, J. Wang, R. He, Y. Ge, Y. Liu, P. K. Chu, X.-F. Yu, *Adv. Sci.* **2023**, *10*, 2204512.

[4] a) W. Qian, X. Xu, J. Wang, Y. Xu, J. Chen, Y. Ge, J. Chen, S. Xiao, S. Yang, *Matter* **2021**, *4*, 942; b) W. G. Li, X. D. Wang, Y. H. Huang, D. B. Kuang, *Adv. Mater.* **2023**, *35*, 2210878.

[5] Y. C. Kim, K. H. Kim, D.-Y. Son, D.-N. Jeong, J.-Y. Seo, Y. S. Choi, I. T. Han, S. Y. Lee, N.-G. Park, *Nature* **2017**, *550*, 87.

[6] S. Deumel, A. van Breemen, G. Gelinck, B. Peeters, J. Maas, R. Verbeek, S. Shanmugam, H. Akkerman, E. Meulenkamp, J. E. Huerdler, M. Acharya, M. García-Batlle, O. Almora, A. Guerrero, G. Garcia-Belmonte, W. Heiss, O. Schmidt, S. F. Tedde, *Nat. Electron.* **2021**, *4*, 681.

[7] H. Tsai, F. Liu, S. Shrestha, K. Fernando, S. Tretiak, B. Scott, D. T. Vo, J. Strzalka, W. Nie, *Sci. Adv.* **2020**, *6*, aay0815.

[8] C. C. Stoumpos, C. D. Malliakas, J. A. Peters, Z. Liu, M. Sebastian, J. Im, T. C. Chasapis, A. C. Wibowo, D. Y. Chung, A. J. Freeman, B. W. Wessels, M. G. Kanatzidis, *Cryst. Growth Des.* **2013**, *13*, 2722.

[9] T. Shi, W. Liu, J. Zhu, X. Fan, Z. Zhang, X. He, R. He, J. Wang, K. Chen, Y. Ge, X. Sun, Y. Liu, P. K. Chu, X.-F. Yu, *Nano Res.* **2023**, *16*, 9983.

[10] a) W. Zhao, J. A. Rowlands, *Med. Phy.* **1995**, *22*, 1595; b) H. Wu, Y. Ge, G. Niu, J. Tang, *Matter* **2021**, *4*, 144; c) S. Kasap, J. B. Frey, G. Belev, O. Tousignant, H. Mani, J. Greenspan, L. Laperriere, O. Bubon, A. Reznik, G. DeCrescenzo, *Sensors* **2011**, *11*, 5112.

[11] M. Xia, Z. Song, H. Wu, X. Du, X. He, J. Pang, H. Luo, L. Jin, G. Li, G. Niu, J. Tang, *Adv. Funct. Mater.* **2022**, *32*, 2110729.

[12] a) C. Liu, Y.-B. Cheng, Z. Ge, *Chem. Soc. Rev.* **2020**, *49*, 1653; b) N. Li, X. Niu, L. Li, H. Wang, Z. Huang, Y. Zhang, Y. Chen, X. Zhang, C. Zhu, H. Zai, Y. Bai, S. Ma, H. Liu, X. Liu, Z. Guo, G. Liu, R. Fan, H. Chen, J. Wang, Y. Lun, X. Wang, J. Hong, H. Xie, D. S. Jakob, X. G. Xu, Q. Chen, H. Zhou, *Science* **2021**, *373*, 561.

[13] Y. Chai, C. Jiang, X. Hu, J. Han, Y. Wang, W. Yang, C. Li, H. Zeng, X. Li, *Small* **2023**, *19*, 2305357.

[14] Z. Song, X. Du, X. He, H. Wang, Z. Liu, H. Wu, H. Luo, L. Jin, L. Xu, Z. Zheng, G. Niu, J. Tang, *Nat. Commun.* **2023**, *14*, 6865.

[15] F. Hao, C. C. Stoumpos, Z. Liu, R. P. H. Chang, M. G. Kanatzidis, *J. Am. Chem. Soc.* **2014**, *136*, 16411.

[16] C. J. Dahlman, R. A. DeCrescent, N. R. Venkatesan, R. M. Kennard, G. Wu, M. A. Everest, J. A. Schuller, M. L. Chabinyc, *Chem. Mater.* **2019**, *31*, 5832.

[17] a) Y. Li, Z. Zhao, F. Lin, X. Cao, X. Cui, J. Wei, *Small* **2017**, *13*, 1604125; b) J.-W. Lee, Z. Dai, C. Lee, H. M. Lee, T.-H. Han, N. De Marco, O. Lin, C. S. Choi, B. Dunn, J. Koh, D. Di Carlo, J. H. Ko, H. D. Maynard, Y. Yang, *J. Am. Chem. Soc.* **2018**, *140*, 6317.

[18] A. Guerrero, J. You, C. Aranda, Y. S. Kang, G. Garcia-Belmonte, H. Zhou, J. Bisquert, Y. Yang, *ACS Nano* **2016**, *10*, 218.

[19] a) A. Kalam, R. Runjhun, A. Mahapatra, M. M. Tavakoli, S. Trivedi, H. Tavakoli Dastjerdi, P. Kumar, J. Lewiński, M. Pandey, D. Prochowicz, P. Yadav, *J. Phys. Chem. C* **2020**, *124*, 3496; b) D. Prochowicz, P. Yadav, M. Saliba, M. Saski, S. M. Zakeeruddin, J. Lewiński, M. Grätzel, *ACS Appl. Mater. Interfaces* **2017**, *9*, 28418.

[20] a) M. Li, B. Li, G. Cao, J. Tian, *J. Mater. Chem. A* **2017**, *5*, 21313; b) Y. Liu, Z. Yang, D. Cui, X. Ren, J. Sun, X. Liu, J. Zhang, Q. Wei, H. Fan, F. Yu, X. Zhang, C. Zhao, S. Liu, *Adv. Mater.* **2015**, *27*, 5176.

[21] J. Chen, J. Lv, X. Liu, J. Lin, X. Chen, *Phys. Chem. Chem. Phys.* **2023**, *25*, 7574.

[22] N. Shrestha, Z. Song, C. Chen, E. Bastola, X. Wang, Y. Yan, R. J. Ellingson, *J. Phys. Chem. Lett.* **2020**, *11*, 121.

[23] a) J. S. Yun, J. Seidel, J. Kim, A. M. Soufiani, S. Huang, J. Lau, N. J. Jeon, S. I. Seok, M. A. Green, A. Ho-Baillie, *Adv. Energy Mater.* **2016**, *6*, 1600330; b) Y. Shao, Y. Fang, T. Li, Q. Wang, Q. Dong, Y. Deng, Y. Yuan, H. Wei, M. Wang, A. Gruverman, J. Shield, J. Huang, *Energy Environ. Mater.* **2016**, *9*, 1752.

[24] a) M. Thompson, S. L. R. Ellison, R. Wood, *Pure Appl. Chem.* **2002**, *74*, 835; b) L. A. Currie, *Anal. Chem.* **1968**, *40*, 586.

[25] a) H. Wu, X. Chen, Z. Song, A. Zhang, X. Du, X. He, H. Wang, L. Xu, Z. Zheng, G. Niu, J. Tang, *Adv. Mater.* **2023**, *35*, 2301406; b) Y. Liu, C. Gao, D. Li, X. Zhang, J. Zhu, M. Wu, W. Liu, T. Shi, X. He, J. Wang, H. Huang, Z. Sheng, D. Liang, X.-F. Yu, H. Zheng, X. Sun, Y. Ge, *Nat. Commun.* **2024**, *15*, 1588.

Supporting Information

Heterogeneous integration of compact perovskite films on pixelated arrays via solid-state crystal growth for X-ray imaging

Tongyu Shi, Jie Kang, Yang Zhang, Wenxuan Yang, Xingzhou Su, Zhiyuan Liu, Xiaoli Wang, Dong Li, Xingchen He, Paul K. Chu, Yanliang Liu, Xue-Feng Yu**

T. Y. Shi, J. Kang, Y. Zhang, W. X. Yang, X. Z. Su, Z.Y. Liu, X.L. Wang, D. Li, X. C. He, Y. L. Liu, Prof. X.-F. Yu

Shenzhen Institute of Advanced Technology, Chinese Academy of Sciences, Shenzhen, Guangdong, 518055, China

T. Y. Shi, Y. L. Liu, Prof. X.-F. Yu

University of Chinese Academy of Sciences, Beijing 100049, China

Y. L. Liu, Prof. X.-F. Yu

Key Laboratory of Biomedical Imaging Science and System, Chinese Academy of Sciences, Shenzhen, Guangdong, 518055, China

Prof. P. K. Chu

Department of Physics, Department of Materials Science and Engineering, and Department of Biomedical Engineering, City University of Hong Kong, Tat Chee Avenue, Kowloon, Hong Kong, China

Corresponding authors: E-mail: yl.liu4@siat.ac.cn (Yanliang Liu) and xf.yu@siat.ac.cn) (Xue-Feng Yu)

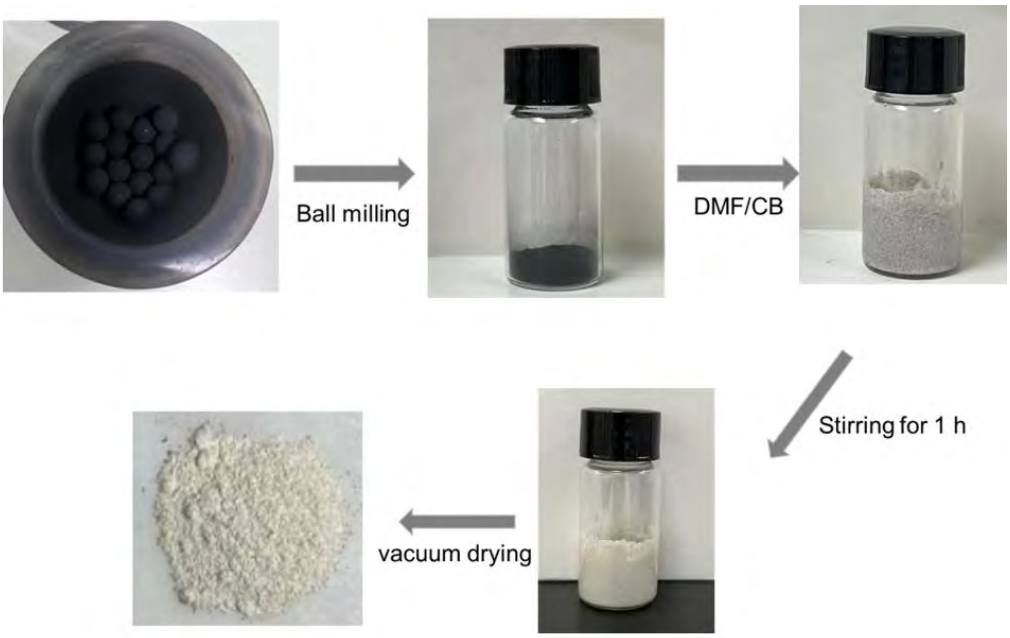

Fig. S1. Schematic illustration of $MAPbI_3$·DMF solvate powder preparation. The $MAPbI_3$ perovskite powders are synthesized by grinding an organic salt (MAI) and lead salt (PbI_2) with a stoichiometric ratio of 1:1 in a planetary ball-milling. The $MAPbI_3$ powder is added to the DMF/CB mixture. After stirring for 1 h, the mixture turns colorless, and the $MAPbI_3$·DMF powder can be obtained by centrifugation and vacuum drying.

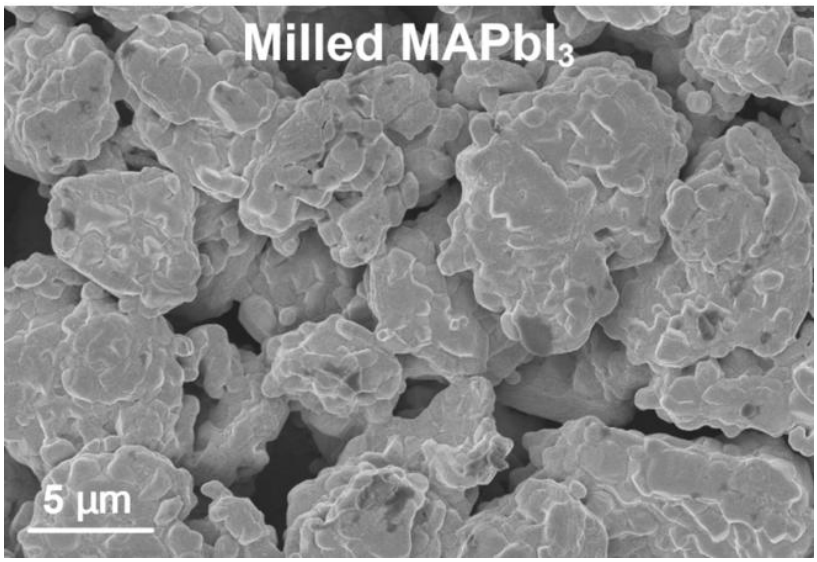

Fig. S2. SEM image of the milled $MAPbI_3$ powder. The ball-milled black perovskite particle exhibits an irregular shape and grain-size distribution.

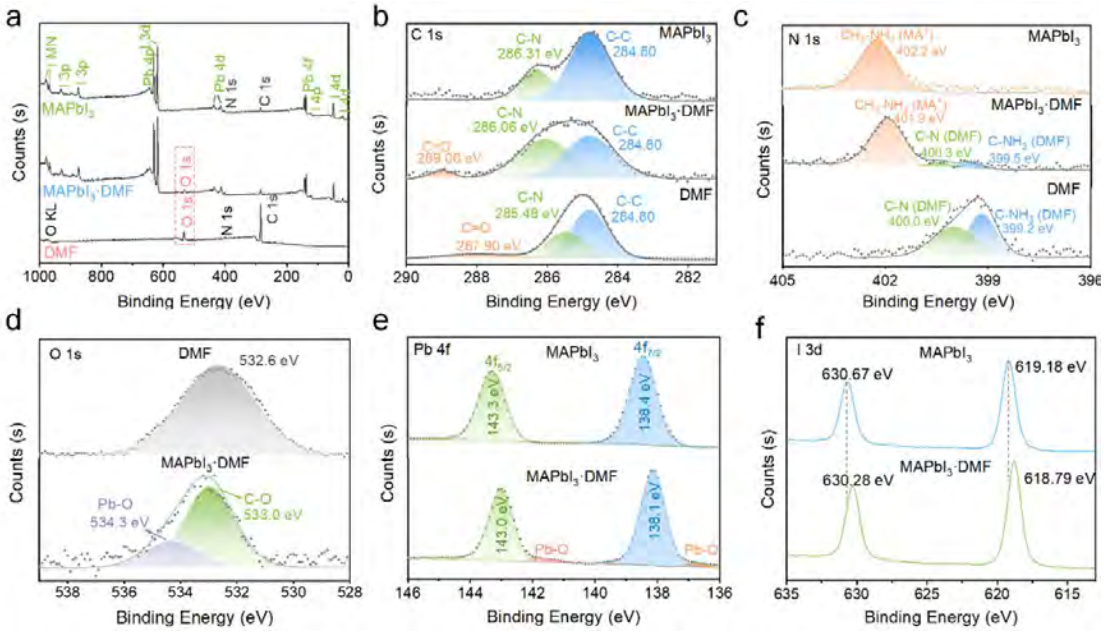

Fig. S3. XPS spectra of $MAPbI_3$·DMF solvate powder. a. XPS survey spectra of milled ·DMF, $MAPbI_3$·DMF, and pure DMF solvent. b. C 1*s* peaks. c. N 1*s* peaks. d. O 1*s* peaks. e. Pb 4*f* peaks. f. I 3*d* peaks.

The chemical composition and formation mechanism of the $MAPbI_3$•DMF powder is investigated by X-ray photoelectron spectroscopy (XPS). As shown in Fig. S3, the XPS survey spectra of both pristine $MAPbI_3$ and the $MAPbI_3$·DMF show the same elements (C, N, I, Pb), but an obviously higher amount of oxygen is observed from $MAPbI_3$·DMF due to the presence of DMF. The C 1*s* spectrum of the solvate can be divided into the typical C-C group, C=O bond, and shifted C-N bond, indicating the incorporation of DMF molecules[1,2]. The N 1*s* peask can be divided into two states of nitrogen belonging to MA^+ and DMF molecules with certain chemical shifts compared to pristine $MAPbI_3$ and DMF. The observed chemical shifts can be attributed to changes in the chemical environment caused by interactions between $MAPbI_3$ and DMF, possibly indicating the formation of intermolecular hydrogen bonding (N-H...O=C asymmetric bifurcated bond) [1]. The O 1s of $MAPbI_3$·DMF can be divided into two peaks at 533.0 eV and 543.3 eV attributable to C-O and Pb-O, respectively[3-4]. Compared with $MAPbI_3$, a decreased binding energy of Pb 4f and two shoulders at 141.7 eV and 136.8 eV in the $MAPbI_3$·DMF can be ascribed to the existence of the bridge Pb–O bond between the $MAPbI_3$ and DMF [5-6].

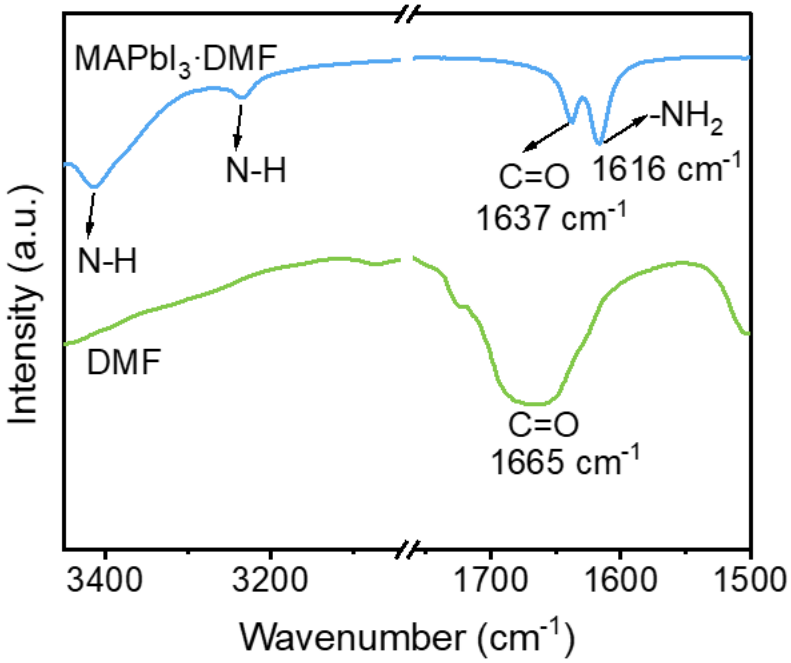

Fig. S4. FTIR spectra of the $MAPbI_3$·DMF solvate powder (blue) and pure DMF solvent (green). The generation of $MAPbI_3$·DMF is evidenced by Fourier transform infrared transmittance spectra (FTIR). The characteristic C═O stretching peak of DMF at 1,665 cm^{-1} downshifts to 1,637 cm^{-1} in $MAPbI_3$·DMF, which can be explained by that the coordination between DMF and $MAPbI_3$ weakens the C=O bond[6-8].As an inorganic compound, PbI_2 shows no functional group vibrations in its FTIR spectrum. MAI, $MAPbI_3$, and $MAPbI_3$·DMF exhibited characteristic vibrational modes of the methylammonium cation. Specifically, the N–H stretching vibrations associated with the NH_3^+ group were observed in the range of 3250-3050 cm^{-1}, while the bending modes of N–H appeared between 1460-1620 cm^{-1}.[9-10] The asymmetric bending vibration of CH_3 was identified at 1420 cm^{-1}, accompanied by a distinct rocking mode of CH_3–NH_3^+ at 1250 cm^{-1}, consistent with the characteristic vibrational signature of organic-inorganic hybrid perovskite systems.[11-12]

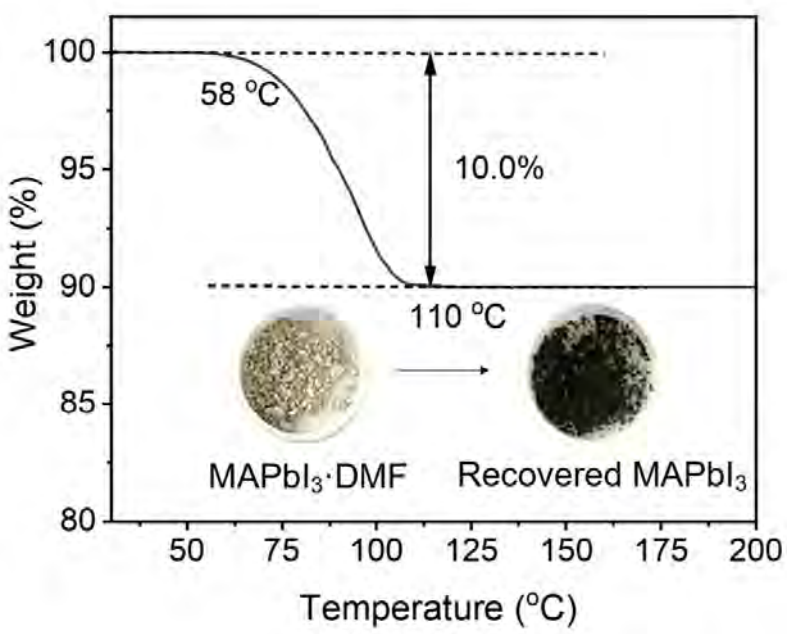

Fig. S5. TGA curve of the $MAPbI_3$·DMF solvate powder. The conversion from $MAPbI_3$·DMF to $MAPbI_3$ is monitored by thermogravimetric analysis, in which the $MAPbI_3$·DMF starts to lose weight at 58 ℃ and is finally converted into $MAPbI_3$ at 110 ℃. The $MAPbI_3$·DMF only loses about 10% of its weight to form recovered $MAPbI_3$, which is in good agreement with the theoretical values of the complete DMF extraction in the molecular formula of $MAPbI_3$·DMF (10.1 %)[13].

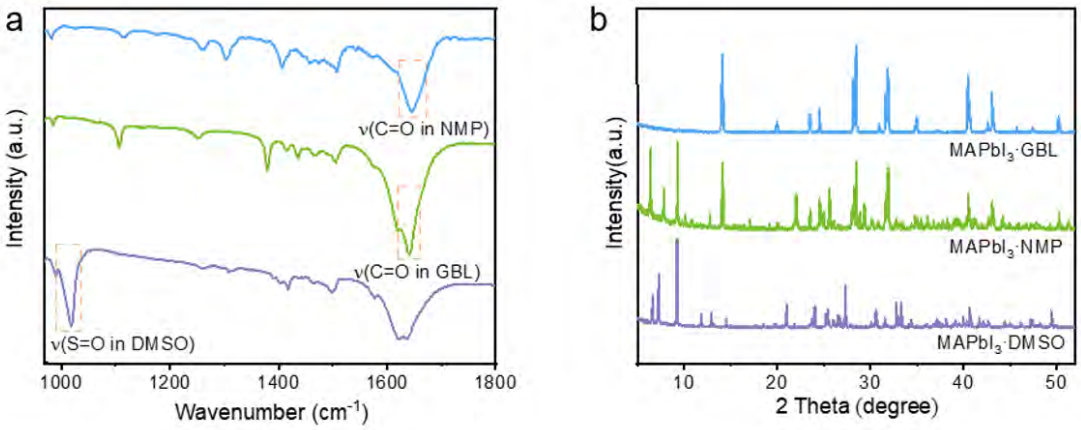

c

Solvent	DMF	DMSO	NMP	GBL
Structure	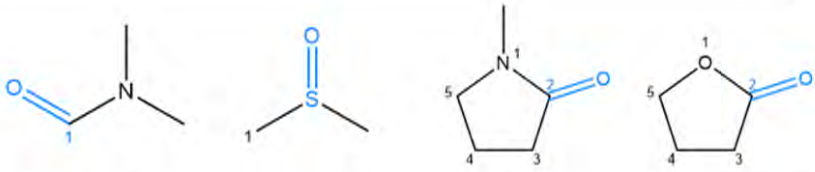			
Polarity	6.4	7.2	6.7	-
IR-solvate *ν*(S=O)/*ν*(C=O)	1637	1017	1642	1647

Fig. S6. Investigation of perovskite solvates formed by other solvents. a. FTIR curves of perovskite solvates. b. XRD patterns of perovskite solvates. c. Summarized parameters of DMF, DMSO, NMP, and GBL solvent. Other solvents are also employed to explore the solvate formation.

Dimethyl sulfoxide (DMSO), γ-butyrolactone (GBL), and 1-methyl-2-pyrrolidinone (NMP) also can form solvates with $MAPbI_3$. Considering the differences in the solvent polarity and steric hindrance in coordination, the solvent coordination ability follows the order of DMSO > DMF > NMP > GBL[14]. Furthermore, different perovskite-solvated adducts can be obtained by substituting different cations (FA) and halide ions in the perovskite composition, proving the universality of the solvent powder preparation method.

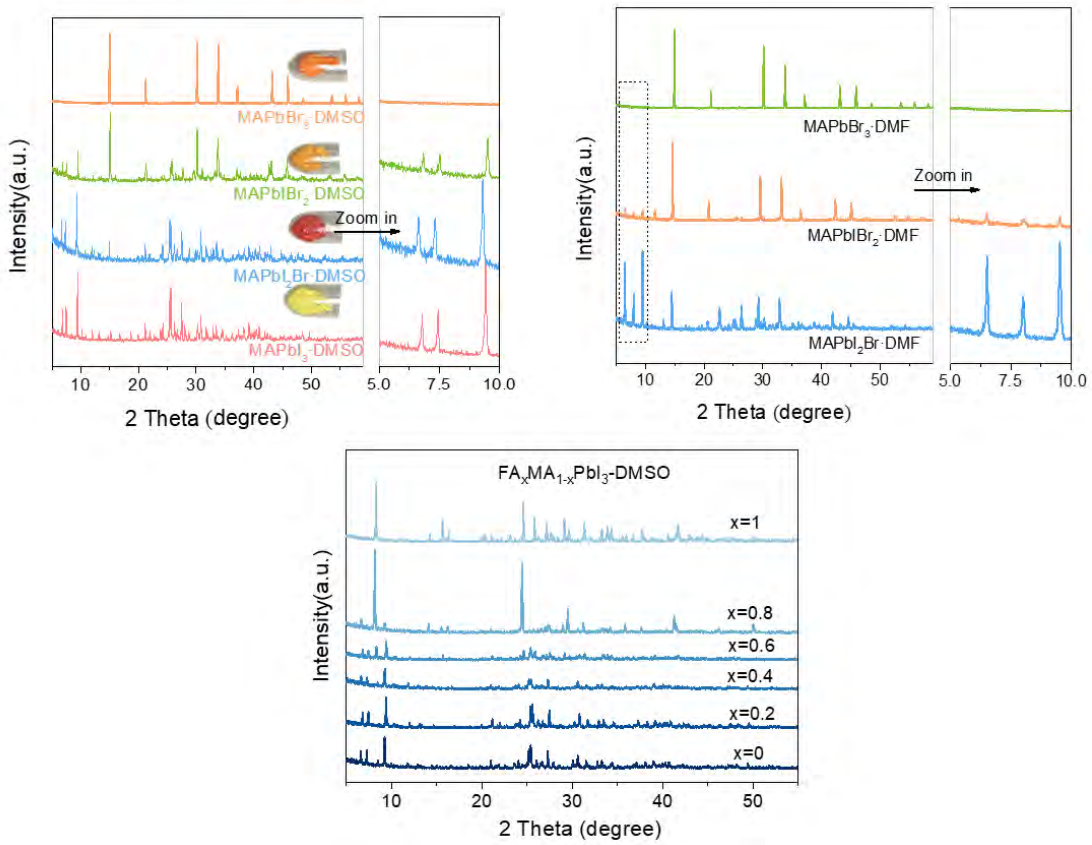

Fig. S7. XRD patterns of perovskite solvates with different components. All the perovskite solvates are synthesized by the same process.

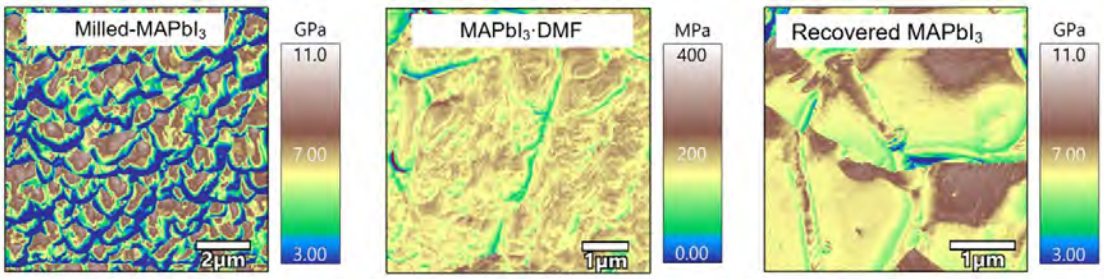

Fig. S8. Young's modulus mapping by Atomic Force Microscope (AFM). Young's modulus of this rod-shape adduct containing crystallization solvent decreased from GPa to the MPa range compared to the pristine perovskite (Milled-$MAPbI_3$). After annealing, the sample exhibits even higher hardness than the pristine stage due to grain growth.

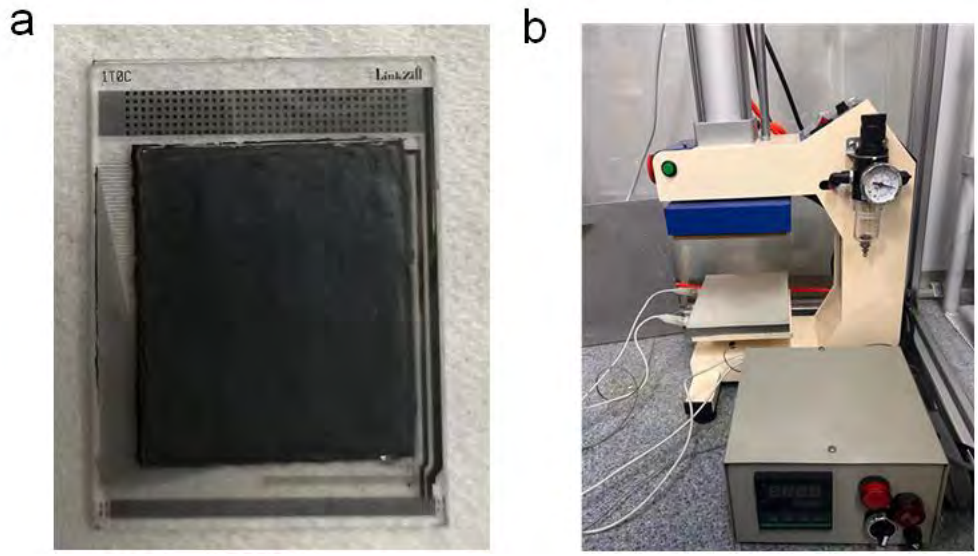

Fig. S9. Photographs of the fabrication process. a. Photograph of $MAPbI_3$ thick film integrated on-chip. b. Self-designed pneumatic hot press machine.

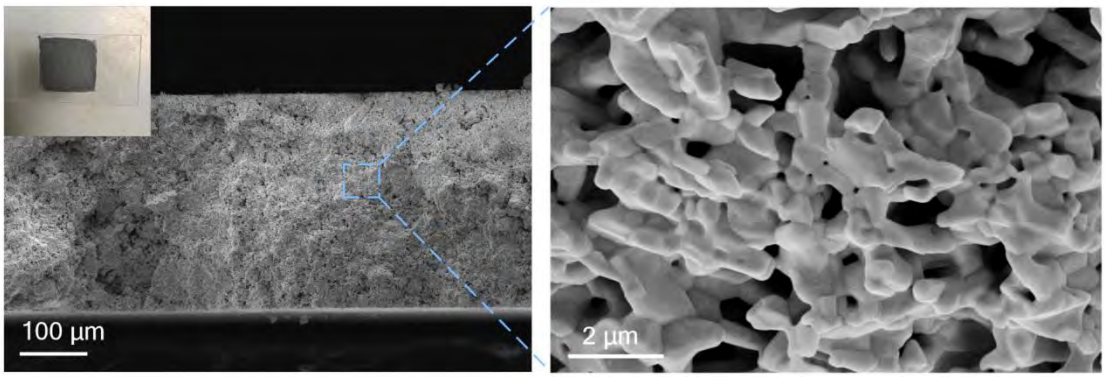

Fig. S10. SEM image of solution-processed $MAPbI_3$ thick films. The solution-processed $MAPbI_3$ thick films are obtained by the blade coating. Inset: photograph of the blade-coated $MAPbI_3$ thick film.

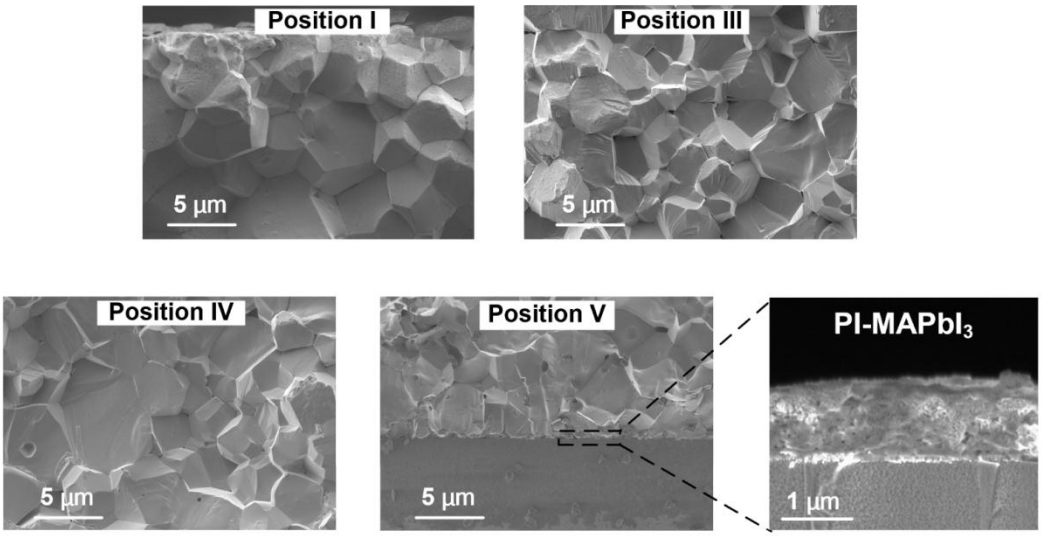

Fig. S11. Cross-section SEM images of soft-pressed $MAPbI_3$ thick film in different areas. The entire cross-section image of the $MAPbI_3$ thick film shows dense and uniform morphology with large grain size, less grain boundaries, and uniform component distribution.

The PI-$MAPbI_3$ layer is spin-coated on the TFT array at 3,000 rpm for 30 s with 100°C annealing for 10 min. The PMDA and ODA (1:0.9) are dissolved in DMF (1:9) and then stirred overnight in a sealed container at room temperature to prepare the polyamide acid (PAA) solution. The $MAPbI_3$ solution is prepared by mixing 4.61 g of PbI_2 and 1.59 g of MAI in 3 mL of DMF and stirring for 6 h. The $MAPbI_3$ solution and PAA solution are mixed with a volume ratio of 1:1 and stirred overnight at room temperature to obtain the PI-$MAPbI_3$ solution.

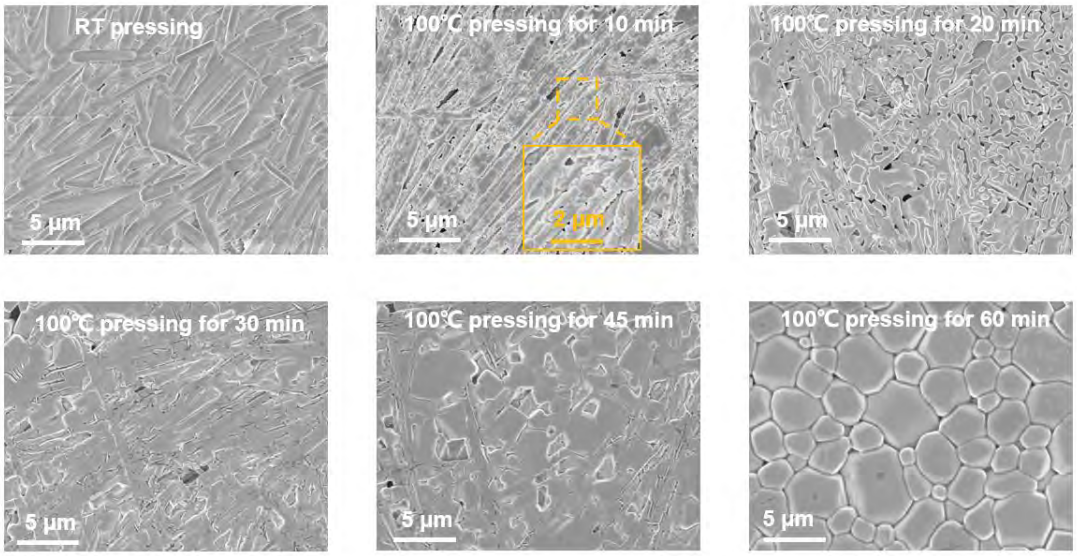

Fig. S12. Morphological evolution of the $MAPbI_3$ thick film during soft pressing. To track hot-pressing induced morphological changes, $MAPbI_3$·DMF films were processed at 100°C/0.8 MPa for 10, 20, 30, 45, and 60 min, followed by ambient cooling and SEM characterization within 2 hours post-processing. The initial $MAPbI_3$·DMF film shows a closely aligned rod-shaped morphology. After annealing, the $MAPbI_3$·DMF solvate transforms gradually into small $MAPbI_3$ grains. The released DMF vapor is able to promote $MAPbI_3$ crystal growth, and the adjacent small $MAPbI_3$ grains merge continuously with each other. Ultimately, the rod-shaped $MAPbI_3$·DMF disappears completely to form a complete $MAPbI_3$ thick film with large grain size and compact morphology.

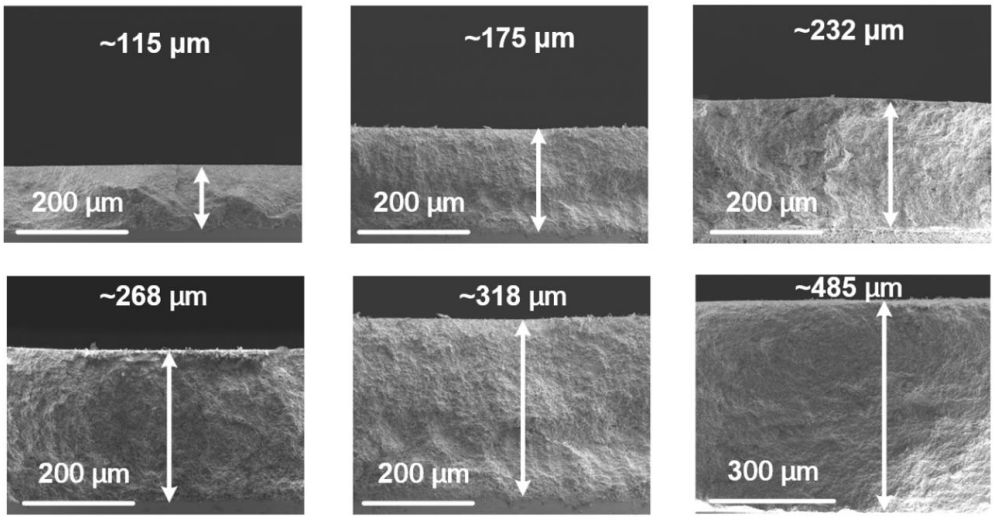

Fig. S13. SEM images of $MAPbI_3$ thick films with different thicknesses. The thickness can be adjusted by controlling the amount of soft-pressed $MAPbI_3 \cdot DMF$ powder and/or the number of lamination cycles.

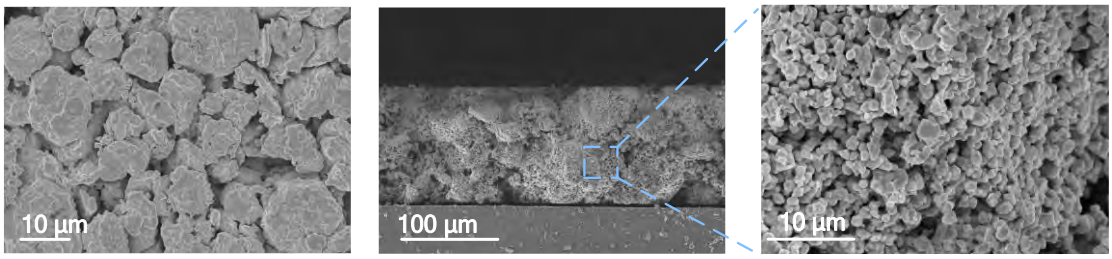

Fig. S14. SEM images of $MAPbI_3$ thick film through directly soft pressing pristine $MAPbI_3$ powder. The $MAPbI_3$ film has a loose structure and cannot be integrated with the substrate, indicating that 0.8 MPa pressure is not enough to rearrange the $MAPbI_3$ powder into the film.

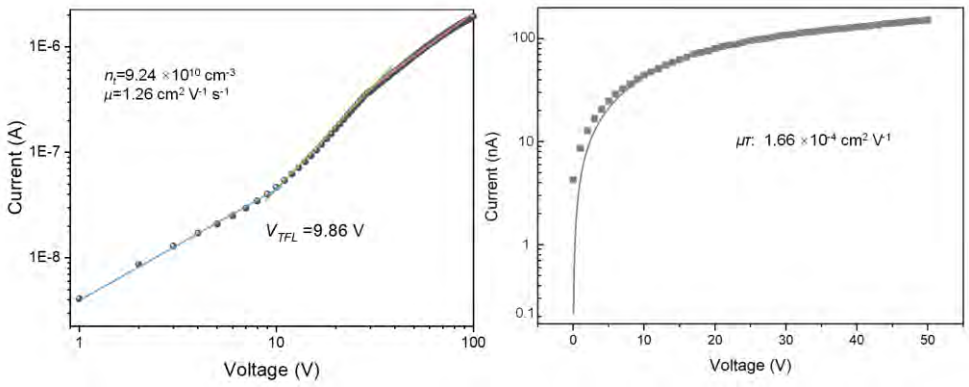

Fig. S15. SCLC characterization and Hecht equation fitted curve of $MAPbI_3$ thick film.

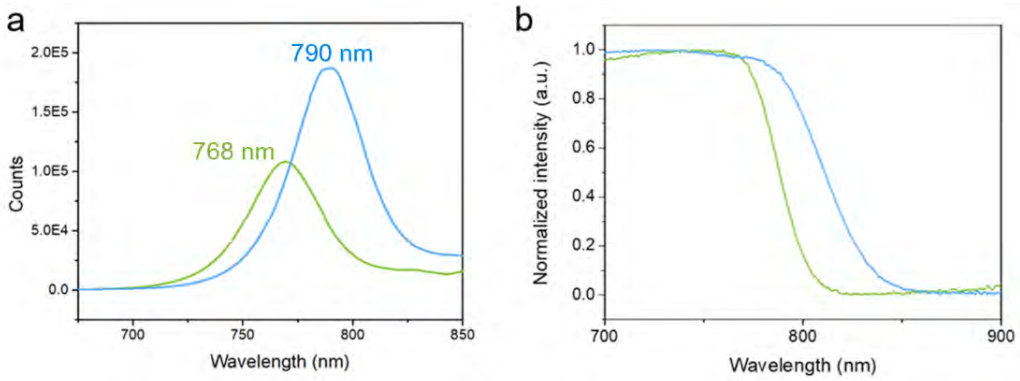

Fig. S16. Optical characterization of $MAPbI_3$ thick films. a. Normalized PL spectra and b. Absorption spectra of the soft-pressed $MAPbI_3$ thick film (blue) and solution-processed $MAPbI_3$ thick film (green). The soft-pressed $MAPbI_3$ thick film shows significantly enhanced photoluminescence (PL) intensity with red-shifted emission peaks from 770 to 790 nm and enlarged time-resolved photoluminescence (TRPL) lifetime in contrast to the conventional solution-processed $MAPbI_3$ thick film.

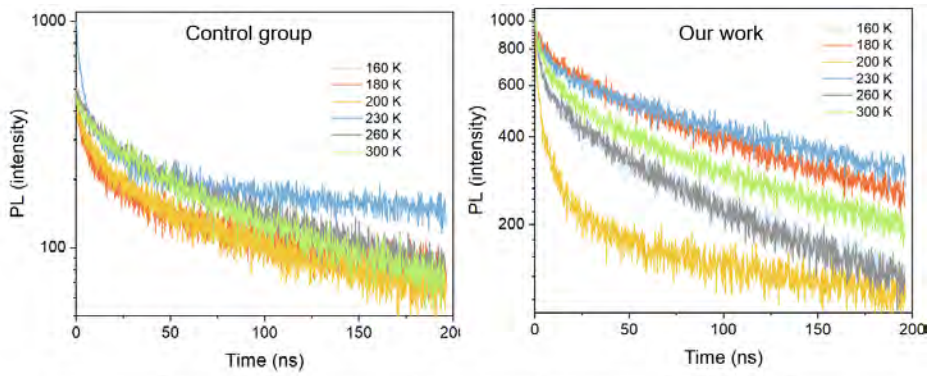

		τ1	τ2		τ1	τ2
160 K	Control group	7.47	70.43	Our work	5.84	98.73
180 K		15.75	76.89		8.23	100.89
200 K		17.73	72.95		9.51	93.88
230 K		18.01	79.60		9.65	123.56
260 K		29.35	81.91		10.12	116.03
300 K		36.52	83.46		11.37	122.44

Fig. S17. TRPL analysis of $MAPbI_3$ at the defect site as a function of temperature.

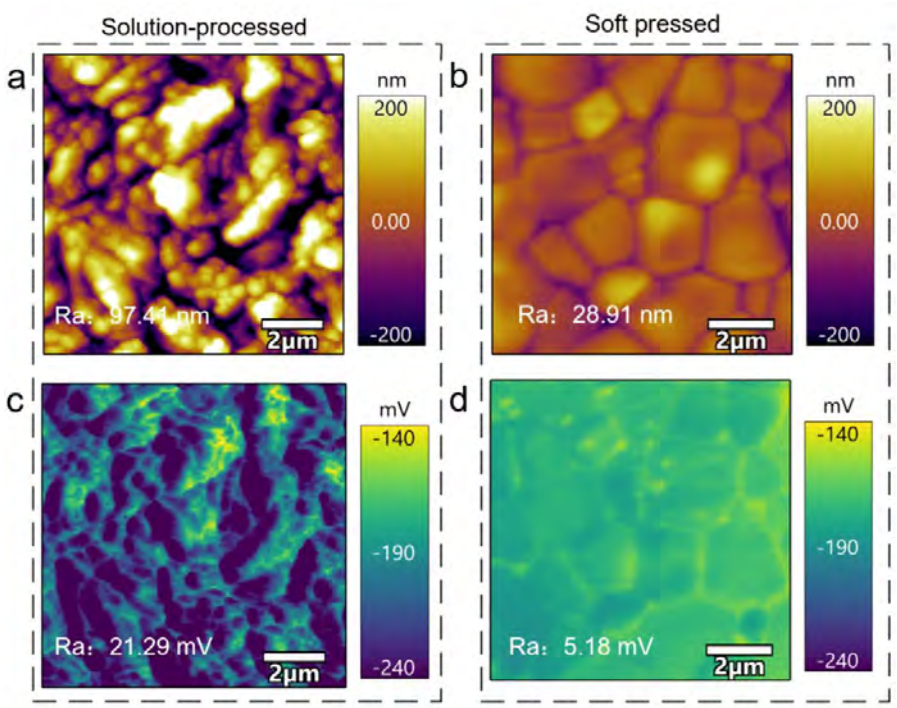

Fig. S18. AFM and KPFM images of the conventional solution-processed $MAPbI_3$ thick film and soft-pressed $MAPbI_3$ thick film. AFM images of a. Solution-processed $MAPbI_3$ thick film and b. Soft-pressed $MAPbI_3$ thick film. KPFM images of c. Solution-processed $MAPbI_3$ thick film and d. Soft-pressed $MAPbI_3$ thick film. The soft-pressed $MAPbI_3$ thick film exhibits a more uniform surface morphology with a larger grain size and lower potential than the conventional solution-processed $MAPbI_3$ thick film.

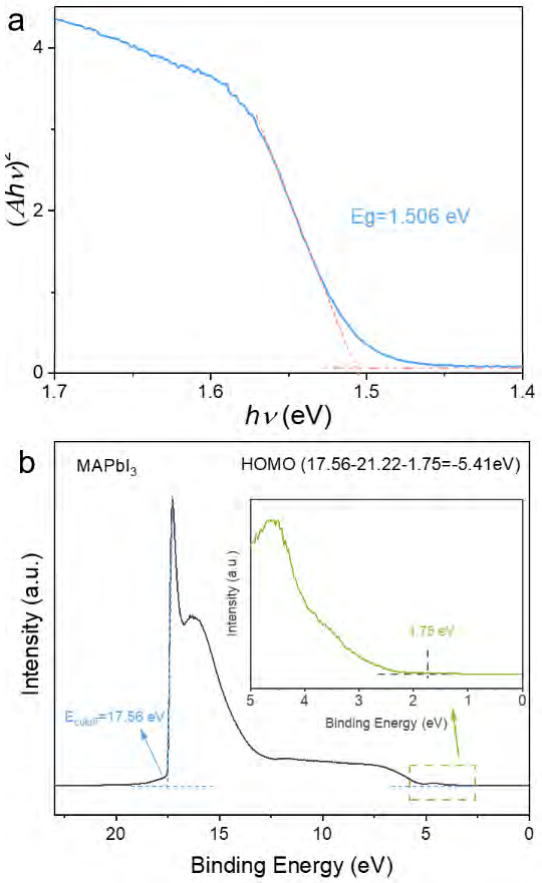

Fig. S19. Energy band structure of the soft-pressed $MAPbI_3$ thick film. a. Tauc plot of our soft-pressed $MAPbI_3$ thick film. b. UPS spectra and energy structure of our soft-pressed $MAPbI_3$ thick film.

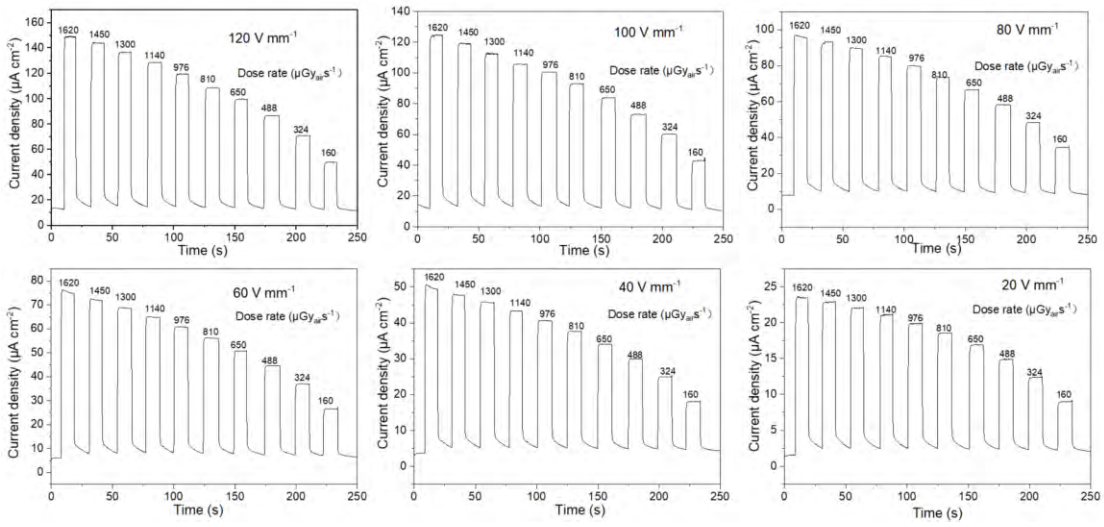

Fig. S20. X-ray response profiles of the X-ray detector at different applied electric fields. The photocurrent densities of the X-ray detector show a good linear relationship with the X-ray dose rates.

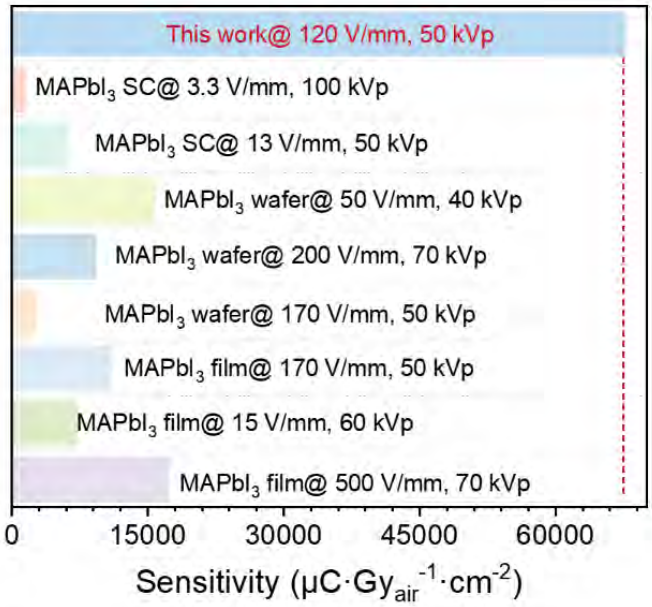

Fig. S21. Summarized sensitivity of reported $MAPbI_3$ X-ray detectors[15-22]. The performance of our X-ray detector significantly surpasses that of other reported $MAPbI_3$-based X-ray detectors.

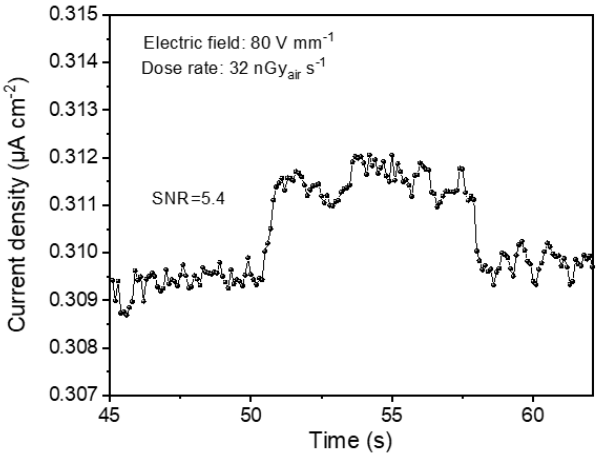

Fig. S22. The response of the X-ray detector at a dose rate of 32 nGy_{air} s^{-1} at 80 V mm^{-1}.

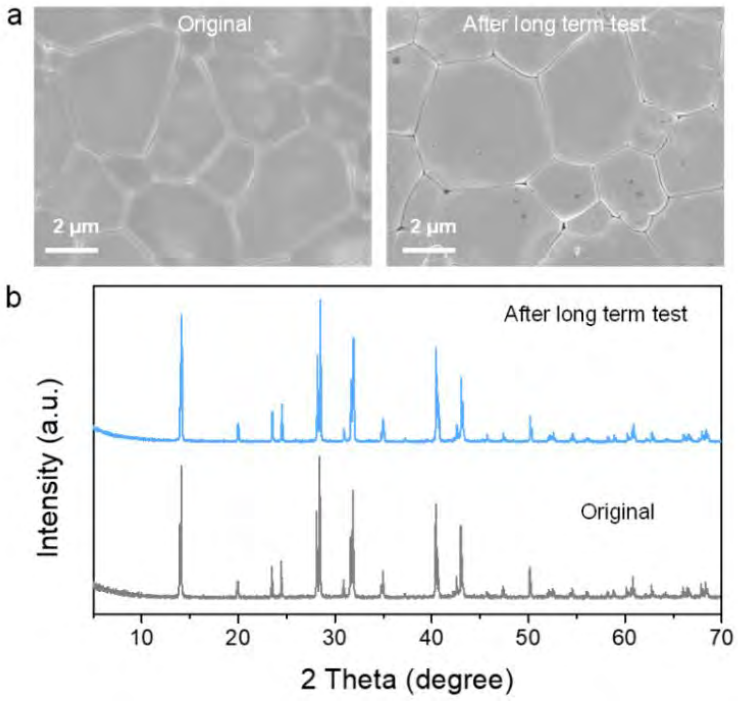

Fig. S23. Investigation of the stability. a). SEM images of the original and long-term tested $MAPbI_3$ film. b). XRD patterns of the original and long-term tested $MAPbI_3$ film.

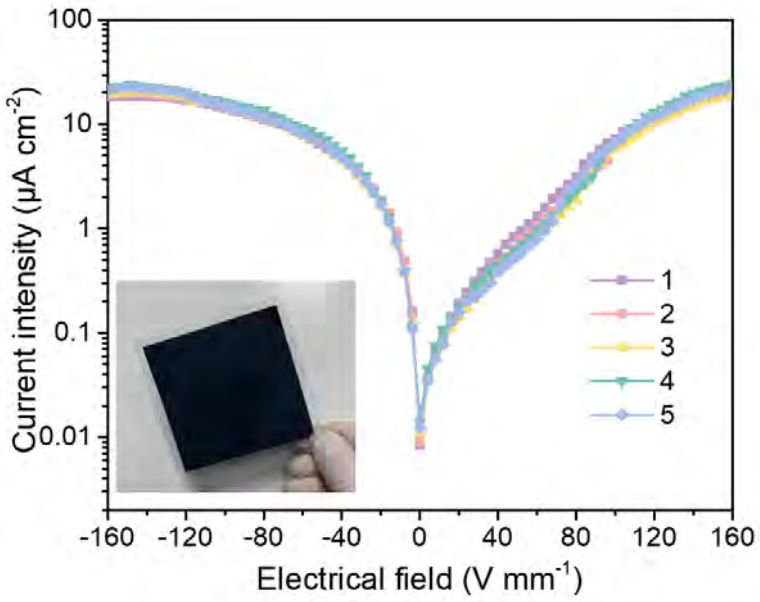

Fig. S24. Characterization of the large-area $MAPbI_3$ X-ray detector. Dark current density-voltages in five random different regions of the large area $MAPbI_3$ detector (inset: photo of the 8 cm×8 cm large-area soft-pressed $MAPbI_3$ thick film).

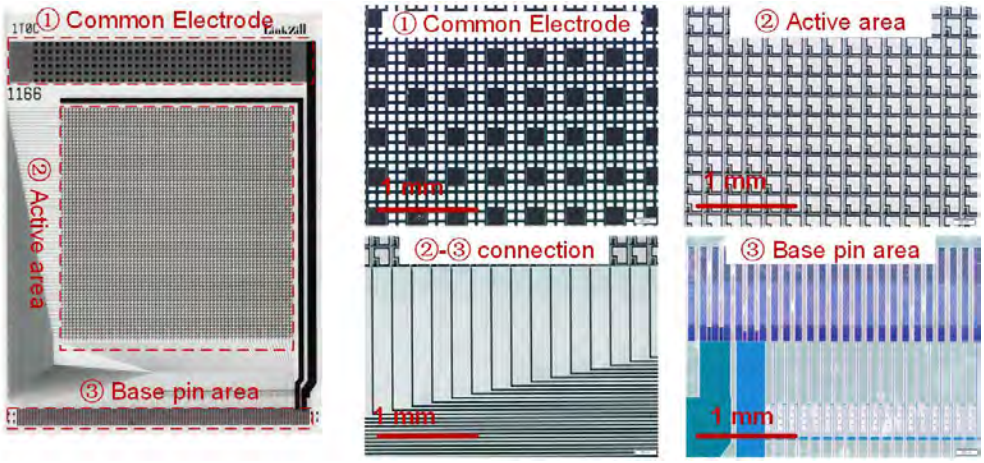

Fig. S25. Photographs of TFT array. The pixel chip mainly includes three regions: common electrode, active area, and base pin area. The size of the TFT array is 17.52 × 23.32 mm^2 with an active area of 12.8 × 12.8 mm^2 (pixel pitch: 200 μm).

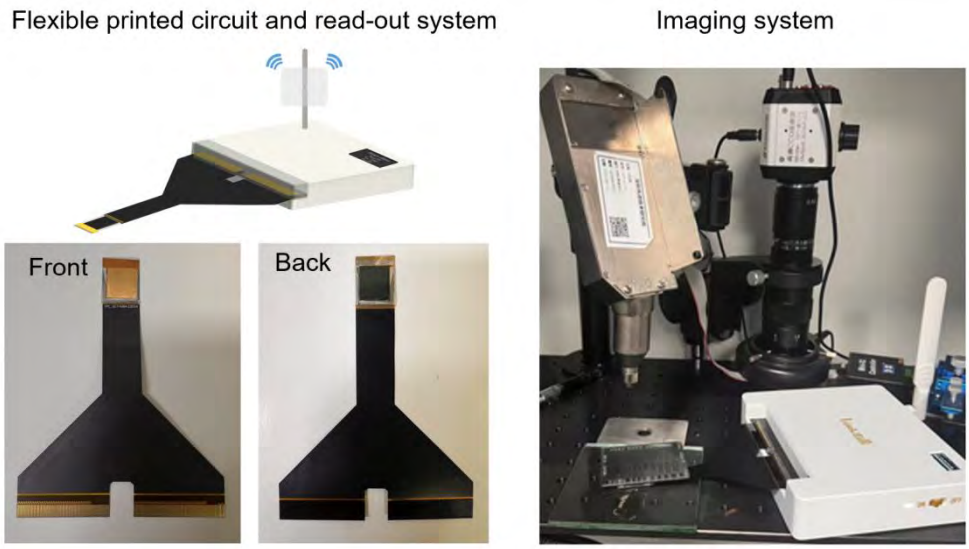

Fig. S26. Photographs of flexible printed circuit and imaging system. The pixelated ITO deposition serves as the bottom electrode for the perovskite photodiodes (pixel pitch: 200 μm), which can be connected to the source electrode of the TFT array *via* the common top Au electrode, allowing bias tuning in the 0-15 V range. Both the perovskite film and the top Au electrode are continuously deposited, so that the area between the photodiodes is determined only by the bottom electrode. The flexible printed circuits consisting of gate drive integrated circuits and readout chips can be thermally bonded onto the TFT substrate for image readout

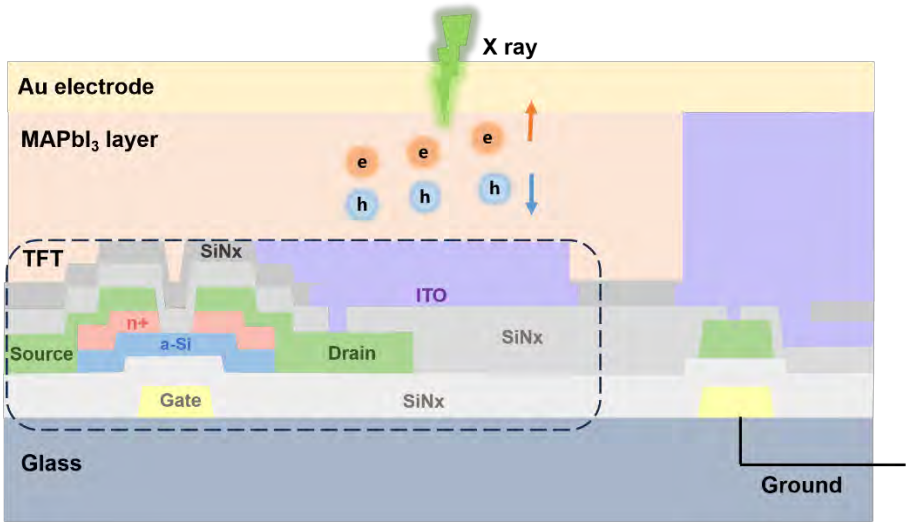

Fig. S27. Schematic cross-section of the perovskite X-ray detector. Upon X-ray irradiation, holes are driven by the external bias and collected by the storage capacitor. The accumulated charge is released and then transferred to the data readout system while the TFT is turned on. After amplification by the backend charge amplifier, the digital image signals are generated by an analog-to-digital converter.

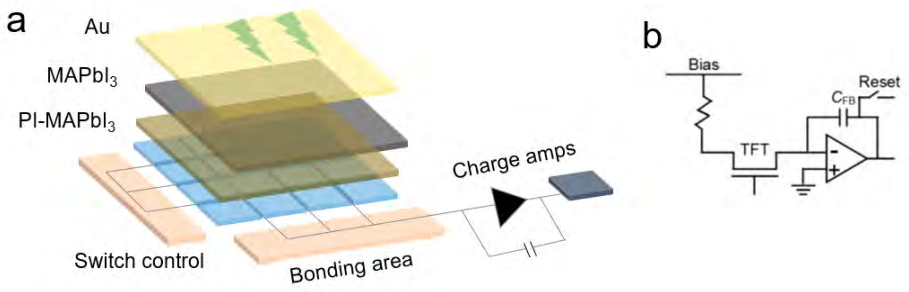

Fig. S28. Structure of the X-ray FPD. a) Schematic illustration of X-ray FPD and b) the architecture of the readout system.

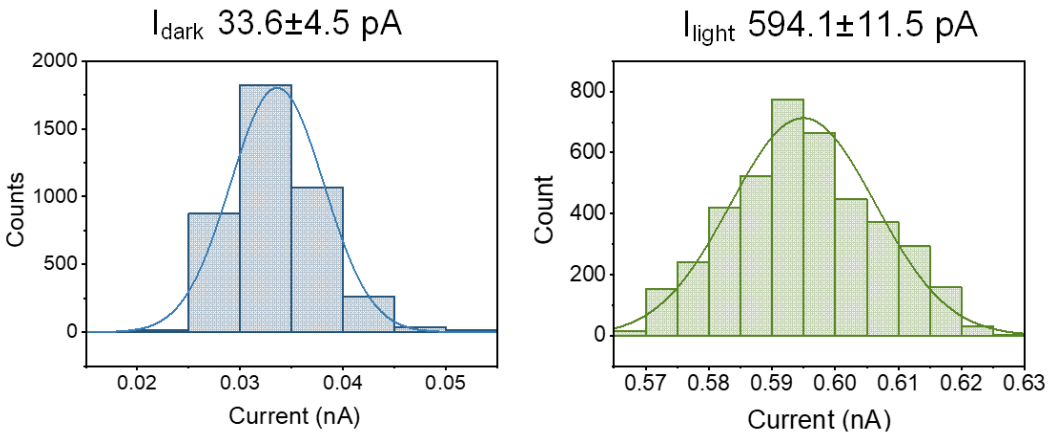

Fig. S29. Dark current and photocurrent distribution of the X-ray imaging panel.

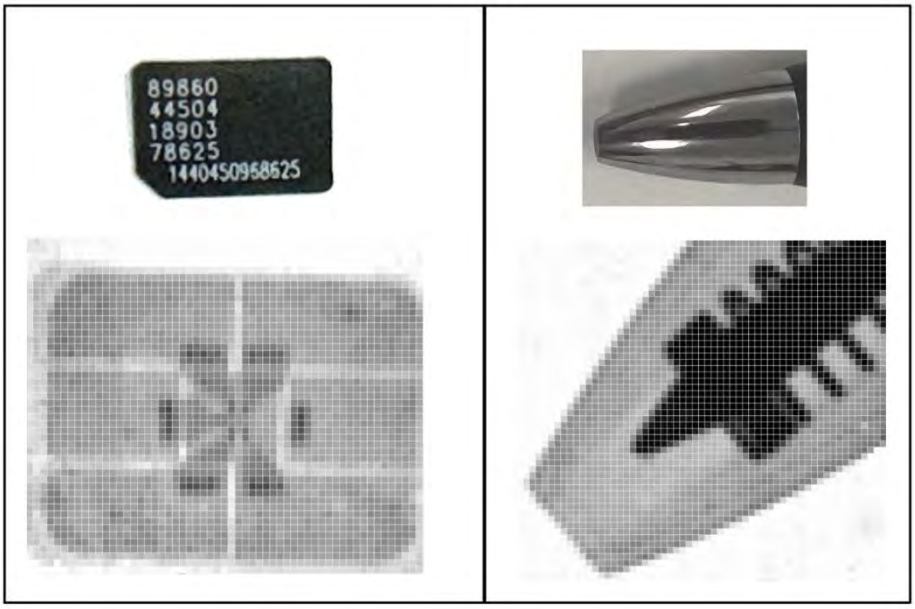

Fig. S30. Photographs and X-ray images of mobile phone memory card and ball-point pen. The X-ray images are recorded under 50 kV X-ray irradiation, without any additional filters between the X-ray tube and the sample. Due to the varying X-ray absorption of the internal metal tip and spring with the outer casing, the contours inside the pen and memory card can be clearly distinguished without damaging the test object.

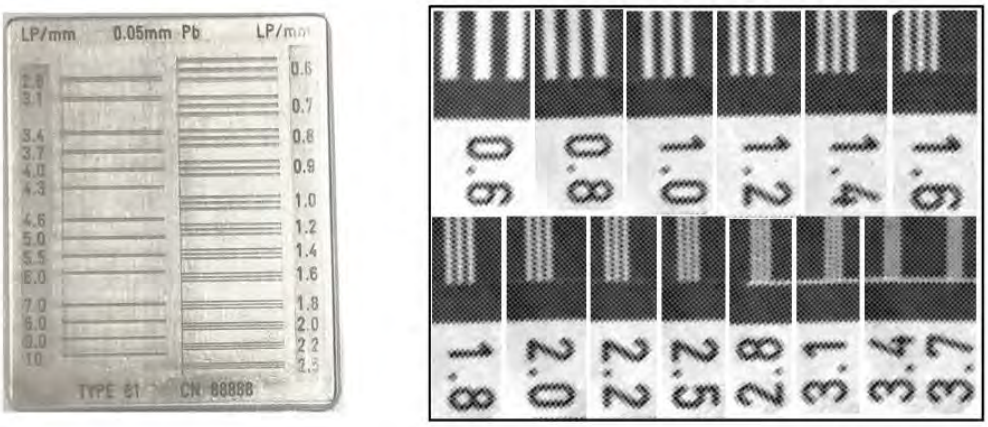

Fig. S31. Photographs and X-ray images of line pair card. The spectral lines with a resolution of 3.1 lp/mm of the standard line pair card can be distinguished under X-ray irradiation

Table S1. Summary of the reported spatial resolution of the perovskite X-ray imaging panel.

	Pixel size (μm)	Resolution (lp/pixel)	Resolution (lp/pixel)	Ref
Perovskite detector	70	3.1	0.22	*Nature*, 2017, 550, 87-91.
	50	3.3	0.16	*Nat. Electron.* 2021, 4, 681-688.
	500	0.92	0.46	*Adv. Mater.* 2023, 35, 2301406
	150	3.4	0.51	*Nat. Commun*. 2023, 14, 6865.
	500	0.86	0.43	*Small* 2023, 19, 2305357
	200	**3.1**	**0.60**	**Our work**

References

1. Hao, F., Stoumpos, C. C., Liu, Z., Chang, R. P. H. & Kanatzidis, M. G. Controllable perovskite crystallization at a gas–solid interface for hole conductor-free solar cells with steady power conversion efficiency over 10%. *J. Am. Chem. Soc.* 136, 16411-16419 (2014).
2. Dahlman, C. J. et al. Controlling solvate intermediate growth for phase-pure organic lead iodide ruddlesden–popper $(C_4H_9NH_3)_2(CH_3NH_3)_{n-1}Pb_nI_{3n+1}$ perovskite thin films. *Chem. Mater.* 31, 5832-5844 (2019).
3. Li, Y. et al. In situ observation of crystallization of methylammonium lead iodide perovskite from microdroplets. *Small* 13, 1604125 (2017).
4. Shi, T. et al. $CsPbBr_3$-DMSO merged perovskite micro-bricks for efficient X-ray detection. *Nano Res.* 16, 9983-9989 (2023).
5. Lee, J.-W. et al. Tuning molecular interactions for highly reproducible and efficient formamidinium perovskite solar cells *via* adduct approach. *J. Am. Chem. Soc.* 140, 6317-6324 (2018).
6. Munir, R. et al. Hybrid perovskite thin-film photovoltaics: in situ diagnostics and importance of the precursor solvate phases. *Adv. Mater.* 29, 1604113, (2017).
7. Yun, Y. et al. Intermediate phase-free process for methylammonium lead iodide thin film for high-efficiency perovskite solar cells. *Adv. Sci*. 8, 2102492, (2021).
8. Liu, W. et al. PbI_2-DMSO assisted in situ growth of perovskite wafers for sensitive direct X-ray detection. *Adv. Sci*. 10, 2204512 (2023).
9. Zhu, Z. et al. Interaction of organic cation with water Molecule in perovskite MAPbI3: from dynamic orientational disorder to hydrogen bonding. *Chem. Mater.* 28, 7385-7393 (2016).
10. Mishra, A., Ahmad, Z., Touati, F., Shakoor, R. A. & Nazeeruddin, M. K. One-dimensional facile growth of $MAPbI_3$ perovskite micro-rods. *RSC Adv.* 9, 11589-11594 (2019).
11. Idígoras, J. et al. The interaction between hybrid organic–inorganic halide perovskite and selective contacts in perovskite solar cells: an infrared spectroscopy study. *Phys. Chem. Chem. Phys.* 18, 13583-13590 (2016).
12. V, N. et al. Unravelling the environmental degradation mechanism of perovskite thin films. *Mater. Adv.* 5, 6426-6439 (2024).
13. Ozaki, M. et al. A Purified, Solvent-intercalated precursor complex for wide-process-window fabrication of efficient perovskite solar cells and modules. *Angew Chem. Int. Edit.* 58, 9389-9393 (2019).
14. Chen, J. et al. Solvent effect on the hole-conductor-free fully printable perovskite solar cells. *Nano Energy* 27, 130-137 (2016).
15. Geng, X. et al. High-performance single crystal $CH_3NH_3PbI_3$ perovskite X-ray detector. *Appl. Phys. Lett.* 118, 063506 (2021).
16. Ye, F. et al. High-quality cuboid $CH_3NH_3PbI_3$ single crystals for high performance X-ray and photon detectors. *Adv. Funct. Mater.* 29, 1806984 (2019).
17. Liu, W. et al. PbI_2-DMSO assisted in situ growth of perovskite wafers for sensitive direct X-ray detection. *Adv. Sci.* 10, 2204512 (2023).
18. Deumel, S. et al. High-sensitivity high-resolution X-ray imaging with soft-sintered metal halide perovskites. *Nat. Electron.* 4, 681-688 (2021).
19. Shrestha, S. et al. High-performance direct conversion X-ray detectors based on sintered hybrid lead triiodide perovskite wafers. *Nat. Photon.* 11, 436-440 (2017).

20. Kim, Y. C. et al. Printable organometallic perovskite enables large-area, low-dose X-ray imaging. *Nature* 550, 87-91 (2017).
21. Qian, W. et al. Solvent engineering of $MAPbI_3$ perovskite thick film for a direct X-ray detector. *Nanoscale* 15, 6664-6672 (2023).
22. Xia, M. et al. Compact and large-area perovskite films achieved *via* soft-pressing and multi-functional polymerizable binder for flat-panel X-ray imager. *Adv. Funct. Mater.* 32, 2110729 (2022).